



**HAL**  
open science

# Inviscid instabilities in rotating ellipsoids on eccentric Kepler orbits

Jérémie Vidal, David Cébron, Nathanaël Schaeffer

► **To cite this version:**

Jérémie Vidal, David Cébron, Nathanaël Schaeffer. Inviscid instabilities in rotating ellipsoids on eccentric Kepler orbits. 2017. hal-01498649v1

**HAL Id: hal-01498649**

**<https://hal.science/hal-01498649v1>**

Preprint submitted on 30 Mar 2017 (v1), last revised 29 Nov 2017 (v2)

**HAL** is a multi-disciplinary open access archive for the deposit and dissemination of scientific research documents, whether they are published or not. The documents may come from teaching and research institutions in France or abroad, or from public or private research centers.

L'archive ouverte pluridisciplinaire **HAL**, est destinée au dépôt et à la diffusion de documents scientifiques de niveau recherche, publiés ou non, émanant des établissements d'enseignement et de recherche français ou étrangers, des laboratoires publics ou privés.



Distributed under a Creative Commons Attribution - NonCommercial - NoDerivatives 4.0 International License

# Inviscid instabilities in rotating ellipsoids on eccentric Kepler orbits

J r mie Vidal<sup>†</sup>, David C bron and Nathana l Schaeffer

Universit  Grenoble Alpes, CNRS, ISTerre, F-38000 Grenoble

(Received xx; revised xx; accepted xx)

Because of their spin and tidal interactions, fluid layers are ellipsoidal in most celestial bodies, such as planets, moons or stars. This departure from a spherical shape can lead to inertial instabilities, and thus volume-filling turbulence. Theoretical studies mainly consider weakly deformed spheres, while experimental or numerical studies use strongly deformed ellipsoids because of technical constraints. To bridge the gap, we present a general and versatile computational framework to perform linear global stability analysis of incompressible flows in arbitrary rotating ellipsoids. We present the uniform vorticity basic flow driven by a mechanical forcing in the limit of vanishing viscosity. Then we describe the inviscid stability analysis method. The latter gives the growth rate and velocity field of the unstable flow. Our framework relies on both symbolic and numeric computations to handle global perturbations of unprecedented complexity. It provides a unified understanding of inertial instabilities in rotating ellipsoids, bringing together and extending several previous studies under a common framework. We apply our method to the case of an orbiting fluid ellipsoid. We recover the two limiting cases, namely the tidally-driven and libration-driven elliptical instabilities. Finally, the general case of an orbiting body on an eccentric Kepler orbit is considered. In this case, several forcing frequencies are present and the ellipsoidal shape of the fluid body evolves in time. These effects give birth to new vigorous orbitally-driven elliptical instabilities.

## 1. Introduction

### 1.1. Geophysical context

Because of gravitational torques generated by their orbital partners, most planets and moons have time-dependent spin rates and ellipsoidal shapes, which disturb their rotational dynamics. It bears the name of mechanical or harmonic forcing (Le Bars *et al.* 2015), such as tides or librations (oscillations of the figure axes of a body with respect to a given mean rotation axis). Librations often occur in synchronized moons as for the Earth's moon (Kopal 1966). Precession refers to the case whereby the instantaneous rotation vector rotates itself about a secondary axis that is fixed in an inertial frame of reference (Poincar  1910). Knowledge of the mechanical forcing and measures of the rotational dynamics of a celestial body allows to infer its internal structure (Dehant & Mathews 2015). Mechanical forcings also play an important role in the dynamics of planetary and stellar liquid interiors, extracting a part of the available rotational energy to sustain large-scale flows (Tilgner 2015) and eventually dynamos. Malkus (1963, 1968, 1989) first pointed out the relevance of harmonic forcings to drive planetary core flows, suggesting that the Earth's magnetic field is maintained by luni-solar precession. Using energy and power considerations, Kerswell (1996) showed that turbulent precession-driven flows are sufficiently vigorous to potentially sustain a dynamo. Numerical dynamos driven by tides

<sup>†</sup> Email address for correspondence: jeremie.vidal@univ-grenoble-alpes.fr

(Barker & Lithwick 2013; Cébron & Hollerbach 2014) and precession (Tilgner 2005, 2007; Wu & Roberts 2009; Goepfert & Tilgner 2016) have been found.

### 1.2. *Inertial instabilities*

More than a century ago, Hough (1895), Sloudsky (1895) and Poincaré (1910) assumed that precession-driven flows depend linearly on Cartesian space coordinates. It simplifies the mathematical complexity of the problem, because flows are then reduced to a time-dependent uniform vorticity (Roberts & Wu 2011). The latter is the order zero response of a rotating fluid enclosed in rigid ellipsoids undergoing mechanical forcings, as confirmed by theoretical and numerical studies of precession (Bondi & Lyttleton 1953; Stewartson & Roberts 1963; Roberts & Stewartson 1965; Busse 1968; Lorenzani & Tilgner 2001; Noir & Cébron 2013). Such nearly uniform vorticity flows are also observed in laboratory precession experiments in the laminar regime (Pais & Le Mouél 2001; Noir *et al.* 2003). Similar conclusions are drawn for librating flows, in both theoretical (Zhang *et al.* 2012; Vantieghem *et al.* 2015), numerical (Favier *et al.* 2015) and experimental studies (Grannan *et al.* 2014).

However a basic flow of uniform vorticity is actually realized only if it is dynamically stable, i.e. if no inviscid perturbation can grow upon the basic state (Kerswell 1993). Otherwise, the basic flow is dynamically unstable and is prone to inertial instabilities. Uniform vorticity basic flows are intrinsically unstable in some regions of the parameter space, as observed for precession-driven flows (Kerswell 1993; Cébron *et al.* 2010*b*; Wu & Roberts 2011), libration-driven flows (Cébron *et al.* 2012*b*; Vantieghem *et al.* 2015) and tidally-driven flows (Kerswell & Malkus 1998; Cébron *et al.* 2010*a*; Le Bars *et al.* 2010; Barker 2016). Finally inertial instabilities are the first ingredient to explain the observed transition towards mechanically-driven turbulence in experiments and simulations (Grannan *et al.* 2014; Favier *et al.* 2015; Grannan *et al.* 2016).

### 1.3. *Motivations*

Previously cited theoretical works have studied inertial instabilities (i) in containers departing very weakly from spheres, (ii) for a subset of simple mechanical forcings and (iii) for rigid ellipsoidal containers. In contrast, (i) laboratory experiments and simulations depart strongly from spherical containers to overcome viscous effects and celestial bodies have mainly triaxial shapes, (ii) celestial bodies are subject to a combination of mechanical forcings and (iii) celestial bodies may deform in time to adjust to gravitational constraints. In this work we relax all these assumptions to perform the inviscid stability analysis of mechanically-driven flows in triaxial ellipsoids subject to arbitrary mechanical forcings.

To take into account the ellipsoidal geometry we perform a global stability analysis. It relies on a Galerkin expansion of the perturbations onto a basis which satisfies the boundary condition(s). Finding an appropriate basis is a difficulty task. Furthermore, complex basis often require advanced numerical schemes (Theofilis 2011). Ellipsoidal harmonics, which are the eigenfunctions of the Laplace operator in ellipsoidal coordinates, form a complete basis (Dassios 2012). Unfortunately, ellipsoidal harmonics have neither explicit expressions, nor known recurrence relationships to generate them. Following Lebovitz (1989) and Wu & Roberts (2011), we use instead a polynomial basis made of Cartesian monomials of various degrees. This basis has two main advantages over other ellipsoidal harmonics: (i) the Cartesian coordinate system is easier to tackle than the ellipsoidal one, and (ii) the basis is explicit and can be generated for any polynomial degree.

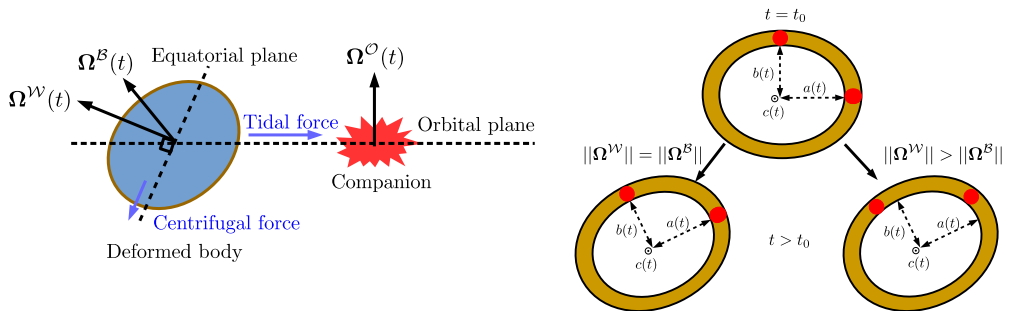


FIGURE 1. (Left) Relevant rotation vectors: the figure axes rotation vector  $\Omega^B$ , the planetary spin rotation vector  $\Omega^W$  and the deforming tidal field rotation vector  $\Omega^O$ , related to  $\Omega^B$  via the planetary rheology. (Right) Physical interpretations of  $\Omega^W$  and  $\Omega^B$ . Top: Equatorial slice of the system at an initial time  $t = t_0$ . The two (red) balls, fixed within the container, are reference points aligned with the ellipsoidal axes at the initial time. At a next time  $t > t_0$ : the bottom left shows the case  $\|\Omega^B\| = \|\Omega^W\|$ , whereas the bottom right shows the case  $\|\Omega^W\| > \|\Omega^B\|$ .

The paper is organized as follows. In section 2 we determine the uniform vorticity basic flow, in the vanishing viscosity limit, driven by any mechanical forcing in arbitrary ellipsoids. In section 3, we describe our method that combines symbolic and numeric computations to extend to higher polynomial degrees the global stability analysis first performed by (Gledzer & Ponomarev 1978, 1992). In section 4, we consider the stability of a fluid in an ellipsoidal container moving along Kepler orbits and describe new orbitally-driven elliptical instabilities (ODEI). We end the paper with a conclusion.

## 2. Governing equations for the basic flow

### 2.1. Model and forcings

We describe a simple model to capture the main dynamics of internal fluid layers of planets and moons undergoing mechanical forcings. We consider a rotating fluid domain (e.g. a planetary liquid core) and assume the fluid is incompressible, of uniform density  $\rho$  and kinematic viscosity  $\nu$ . This fluid domain is enclosed in an arbitrary solid container (e.g. a planetary solid mantle). The shape of the container may depend on time  $t$ . A flow is driven in the fluid cavity through mechanical coupling at its boundary. The fluid boundary  $\mathcal{S}$  is modeled as a triaxial ellipsoid of principal semi-axes denoted  $(a(t), b(t), c(t))$  and of volume  $4\pi abc/3$ . The center of mass of the triaxial fluid cavity  $O$  is chosen as the origin of our working frames.

Figure 1 (Left) depicts the physical situation, showing the planetary triaxial cavity filled with fluid. Focusing on the fluid boundary  $\mathcal{S}$ , we define two rotation vectors in the inertial frame of reference considered here. The first one is the rotation vector  $\Omega^W(t)$  of the boundary (mantle rotation vector in planetary terms). The plane perpendicular to  $\Omega^W(t)$  and enclosing  $O$  is the equatorial plane. For planetary layers, this rotation naturally leads to a centrifugal force. The latter generates an equatorial bulge and deforms the boundary into a spheroidal (axisymmetric) fluid boundary. Besides, the tidal field due to an orbiting companion generates a tidal bulge and the boundary becomes a triaxial ellipsoid of semi-axes  $(a(t), b(t), c(t))$ . So we define a second rotation vector, denoted  $\Omega^B(t)$ , which describes the rotation of the principal figure semi-axes  $(a(t), b(t), c(t))$  of the ellipsoidal fluid domain. In the frame rotating at the spin velocity  $\Omega^B(t)$ , the fluid

boundary equation is

$$(\mathcal{S}) : \left( \frac{x}{a(t)} \right)^2 + \left( \frac{y}{b(t)} \right)^2 + \left( \frac{z}{c(t)} \right)^2 = 1. \quad (2.1)$$

Here, the semi-axes may change in time because of the time-dependence of the tidal field (e.g. if the orbit of the orbiting companion is eccentric). Note also that the rotation vector  $\boldsymbol{\Omega}^{\mathcal{B}}(t)$  of the figure axes is directly related to the orbital rotation vector  $\boldsymbol{\Omega}^{\mathcal{O}}(t)$  of the orbiting companion. This relation depends among other things on the rheology of the container, i.e. how quick does the solid shape respond to the internal and external forcings. The orbital rotation vector defines the companion orbital plane, which is orthogonal to  $\boldsymbol{\Omega}^{\mathcal{O}}(t)$ . These two rotation vectors are associated with two reference frames. The body frame (also called frame of figure) is the frame rotating at  $\boldsymbol{\Omega}^{\mathcal{B}}(t)$ , whereas the mantle frame is rotating at  $\boldsymbol{\Omega}^{\mathcal{W}}(t)$  with respect to the inertial frame.

As a result, vector  $\boldsymbol{\Omega}^{\mathcal{B}}(t)$  corresponds to a block rotation of the ellipsoidal shape, while vector  $\boldsymbol{\Omega}^{\mathcal{W}}(t)$  is the angular velocity of a material particle at the ellipsoidal boundary. Figure 1 (Right) illustrates these differences. The equatorial slice of the system is represented at two different times. At  $t = t_0$ , two red dots are attached with the ellipse made by  $a(t)$  and  $b(t)$ . They may represent a geophysical feature of  $\mathcal{S}$ , such as a mountain ridge. At time  $t > t_0$ , both the container and the mantle materials have rotated. Two cases are drawn. If  $\|\boldsymbol{\Omega}^{\mathcal{B}}\| = \|\boldsymbol{\Omega}^{\mathcal{W}}\|$ , then the two points stay attached to the principal axes. If  $\|\boldsymbol{\Omega}^{\mathcal{W}}\| > \|\boldsymbol{\Omega}^{\mathcal{B}}\|$ , then the figure axes rotate slower than the boundary. The two dots are now displaced from the figure axes. It shows that the two rotation vectors play a different role and must be distinguished in the general case.

In the following we choose  $L = \sqrt{(a^2 + b^2)}/2$  as the length scale. We choose the time scale  $\Omega_s^{-1}$ , such that the time-averaged value of  $\|\boldsymbol{\Omega}^{\mathcal{W}}(t)\|$  in absence of any mechanical forcing is unitary. For clarity, the dimensionless variables will be also noted as their dimensional counterparts. In fluid mechanics studies, the knowledge of  $(a(t), b(t), c(t))$ ,  $\boldsymbol{\Omega}^{\mathcal{B}}(t)$  and  $\boldsymbol{\Omega}^{\mathcal{W}}(t)$  is sufficient to fully determine the forcing acting on the fluid. In Appendix A we present some forcings previously used in fluid mechanics.

## 2.2. Uniform vorticity component of mechanically-driven basic flow

The knowledge of basic flow solutions of the governing Navier-Stokes equation is essential to instability studies. We work in the body reference frame where the fluid boundary is given by equation (2.1). Mechanical forcings drive a basic flow  $\mathbf{U}(\mathbf{r}, t)$ , which is incompressible ( $\nabla \cdot \mathbf{U} = 0$ ) and satisfies the impermeability boundary condition  $\mathbf{U} \cdot \mathbf{n} = 0$  at  $\mathcal{S}$ , where  $\mathbf{n}$  is the unitary outward vector normal to  $(\mathcal{S})$ . Following the seminal work of Poincaré (1910), we assume that  $\mathbf{U}$  is a laminar flow of time-dependent and uniform vorticity  $2\mathbf{q}$ . In the body frame these flows are of the form (Noir & Cébron 2013)

$$\mathbf{U} = \begin{pmatrix} 0 & -2a^2q_z/(a^2 + b^2) & 2a^2q_y/(a^2 + c^2) \\ 2b^2q_z/(a^2 + b^2) & 0 & -2b^2q_x/(b^2 + c^2) \\ -2c^2q_y/(a^2 + c^2) & 2c^2q_x/(b^2 + c^2) & 0 \end{pmatrix} \cdot \begin{pmatrix} x \\ y \\ z \end{pmatrix} \quad (2.2)$$

with  $\mathbf{r} = (x, y, z)^T$  the position vector and  $(q_x, q_y, q_z)^T$  the Cartesian components of the time-dependent fluid rotation rate  $\mathbf{q}$ . Basic flow (2.2) It is an exact solution of the nonlinear, viscous, vorticity equation in the body frame with the boundary condition  $\mathbf{U} \cdot \mathbf{n} = 0$ . With such a boundary condition, the permanent regime of the inviscid basic flow is entirely dependent on the chosen initial condition (see Tilgner 2015). In order to

obtain a unique solution, independent of the initial vorticity, viscous coupling with the boundary is needed.

We thus introduce the Ekman number (dimensionless viscosity)  $E = \nu/(\Omega_s L^2)$ . In the low viscosity asymptotic limit  $E \ll 1$ , we follow Busse (1968) and consider the uniform vorticity basic flow (2.2) as an accurate approximation of the mainstream flow in the bulk of the cavity. However, this flow does not satisfy the no-slip boundary condition. An exact description of the Ekman boundary layer in a triaxial ellipsoid for an arbitrary mechanical forcing is out of reach. We adopt instead a simple linear model, similar to the one of Åkervik *et al.* (2006). They add in the governing equation a linear term, proportional to the difference between the velocity perturbation and a (well-chosen) target, to compute steady (basic) flows of Navier-Stokes equation for flow-control purposes. The model we choose, originally developed for precessing ellipsoids (Noir & Cébron 2013), is in good agreement with the nonlinear leading order viscous solution of Busse (1968). We parametrize viscous effects by adding a linear dissipative term in the inviscid vorticity equation. In the body frame this term is (in dimensionless form)

$$E^{1/2} \underbrace{\begin{pmatrix} \lambda_r & -\lambda_i & 0 \\ \lambda_i & \lambda_r & 0 \\ 0 & 0 & \lambda_r \end{pmatrix}}_{\mathcal{D}} \left[ \mathbf{q} - (\boldsymbol{\Omega}^W - \boldsymbol{\Omega}^B) \right], \quad (2.3)$$

with  $\boldsymbol{\Omega}^W - \boldsymbol{\Omega}^B$  the wall rotation vector in the body frame. Damping term (2.3) is thus proportional to the differential rotation between the fluid and the wall. In formula (2.3)  $\lambda_r < 0$  and  $\lambda_i$  are free parameters, actually related to the real and the imaginary parts of the damping factor of the only uniform vorticity inertial mode, i.e. the so-called spin-over mode (for details see Noir & Cébron 2013). Their specific values are unimportant here since the viscous torque (2.3) is only considered in the vanishing viscosity limit, where it can be neglected compared to the pressure torque. The viscous torque determines uniquely the inviscid rotation rate  $\mathbf{q}$  in the limit  $E^{1/2} \rightarrow 0$ . The full governing vorticity equation of the basic flow becomes

$$\frac{d\mathbf{q}}{dt} - \left[ (\mathbf{q} + \boldsymbol{\Omega}^B) \cdot \nabla \right] \mathbf{U} = -\frac{d\boldsymbol{\Omega}^B}{dt} + E^{1/2} \mathcal{D} \left[ \mathbf{q} - (\boldsymbol{\Omega}^W - \boldsymbol{\Omega}^B) \right]. \quad (2.4)$$

### 3. Inviscid global stability analysis

#### 3.1. Polynomial expansion

We investigate whether basic flows of uniform vorticity driven by mechanical forcings in rigid ellipsoidal containers are stable against small perturbations. To perform a linear stability analysis, we expand the total velocity field into the sum of the basic flow  $\mathbf{U}$  and a perturbation  $\mathbf{u}$ . The linearized governing equations for the perturbation are

$$\frac{\partial \mathbf{u}}{\partial t} + (\mathbf{U} \cdot \nabla) \mathbf{u} + (\mathbf{u} \cdot \nabla) \mathbf{U} + 2 \boldsymbol{\Omega}^B \times \mathbf{u} = -\nabla \pi, \quad (3.1)$$

$$\nabla \cdot \mathbf{u} = 0, \quad (3.2)$$

with  $\pi$  the reduced pressure. The basic flow  $\mathbf{U}$  is linearly unstable if the amplitude  $\|\mathbf{u}\|$  grows without any bound with evolving time. To remove the pressure term, we take the curl of equation (3.1) and obtain the governing equation for the rotation rate  $\boldsymbol{\zeta} = (\nabla \times \mathbf{u})/2$  of the perturbation

$$\frac{\partial \boldsymbol{\zeta}}{\partial t} + (\mathbf{U} \cdot \nabla) \boldsymbol{\zeta} + (\mathbf{u} \cdot \nabla) \boldsymbol{\omega} - (\boldsymbol{\zeta} \cdot \nabla) \mathbf{U} = \left( \boldsymbol{\omega} + \boldsymbol{\Omega}^B \right) \cdot \nabla \mathbf{u}. \quad (3.3)$$

As originally devised by Gledzer & Ponomarev (1978, 1992), if  $\mathbf{u}$  is a Cartesian polynomial of degree  $n$  in the coordinates  $(x, y, z)$ , then each term in equation (3.3) is a polynomial in the Cartesian coordinates of maximum degree  $n - 1$ . This suggests to look for perturbations  $\mathbf{u}$  which belongs to a finite-dimensional vector space of Cartesian polynomials.

We consider the finite-dimensional vector space  $\mathcal{V}_n$ , such that an element  $\mathbf{u} \in \mathcal{V}_n$  is of maximum degree  $n$  and satisfies  $\mathbf{u} \cdot \mathbf{n} = 0$  at the solid boundary  $\mathcal{S}$  and  $\nabla \cdot \mathbf{u} = 0$ . The dimension of  $\mathcal{V}_n$  is (Lebovitz 1989; Vantieghem 2014)

$$\dim \mathcal{V}_n = n(n+1)(2n+7)/6. \quad (3.4)$$

Vector space  $\mathcal{V}_n$  is invariant under the momentum equation (3.1), as shown in triaxial geometry by Lebovitz (1989) (see also Kerswell 1993, for the particular case of spheroids). Thus we consider perturbations  $\mathbf{u} \in \mathcal{V}_n$ .

Following Lebovitz (1989) the basis elements of  $\mathcal{V}_n$ , denoted  $\{\mathbf{v}_i(\mathbf{r})\}$ , are

$$\mathbf{v}_i(\mathbf{r}) = \nabla(p_i F) \times \hat{\mathbf{x}}, \quad \mathbf{v}_{N_2+i}(\mathbf{r}) = \nabla(p_i F) \times \hat{\mathbf{y}} \text{ for } i \in [1, N_2] \quad (3.5)$$

and

$$\mathbf{v}_{2N_2+i}(\mathbf{r}) = \nabla(p_i F) \times \hat{\mathbf{z}} \text{ for } i \in [1, N_1] \quad (3.6)$$

with  $p_i$  a polynomial of degree  $n - 1$  or less,  $(\hat{\mathbf{x}}, \hat{\mathbf{y}}, \hat{\mathbf{z}})$  the unit basis vectors in Cartesian geometry,

$$N_1 = \frac{1}{2}n(n+1), \quad N_2 = \frac{1}{6}n(n+1)(n+2) \quad (3.7)$$

and

$$F = 1 - \frac{x^2}{a^2} - \frac{y^2}{b^2} - \frac{z^2}{c^2}. \quad (3.8)$$

The total number of these vectors is given by (3.4). In practice, we choose

$$\{p_i\} = \left\{ \underbrace{1, x, y, x^2, xy, y^2, \dots, x^{n-1}, y^{n-1}}_{i \in [1, N_1]}, \underbrace{z, xz, yz, z^2, \dots, z^{n-1}}_{i \in [N_1+1, N_2]} \right\}. \quad (3.9)$$

The polynomial set (3.9) ensures that basis elements (3.5) - (3.6) are linearly independent. Using this procedure, we have effectively build polynomial basis for  $n$  as large as 25.

Note that we have also considered and implemented another algorithm to build the vector space  $\mathcal{V}_n$  for arbitrary  $n$ . as described in Appendix B. However it was less efficient to the above procedure.

### 3.2. Stability problem

We expand the perturbation  $\mathbf{u}(\mathbf{r}, t)$  as a linear combination of the basis elements of  $\mathcal{V}_n$ , i.e.

$$\mathbf{u}(\mathbf{r}, t) = \sum_{i=1}^{\dim \mathcal{V}_n} \alpha_i(t) \mathbf{v}_i(\mathbf{r}) \quad (3.10)$$

where  $\{\alpha_i(t)\}$  is a set of arbitrary time-dependent coefficients. The expansion (3.10) reduces the stability problem (3.3) to a finite number of ordinary differential equations.

Following Wu & Roberts (2011), we substitute the expansion (3.10) into the vorticity equation (3.3) and set to zero the pre-factor of each monomial  $x^i y^j z^k$  (with  $i + j + k \leq n$ ) in each Cartesian component of the vorticity equation, because it holds for any position  $(x, y, z)$  in space (the monomials are mutually orthogonal). It leads to a system

of  $n(n+1)(n+2)/2$  linear equations, whose unknowns are  $\{\alpha_i(t)\}$  and their first time derivative. Note that this system of equations is not linearly independent yet. Indeed, since  $\nabla \cdot \boldsymbol{\zeta} = 0$  the divergence of (3.3) imposes that  $n(n-1)(n+1)/6$  of these equations are automatically satisfied. They are associated with the pre-factors of the the monomials which do not disappear after taking the divergence. Dropping the latter equations leads to a set of  $n(n+1)(2n+7)/6$  linearly independent equations, in agreement with the dimension (3.4). It is a time-dependent system written in matrix form

$$\frac{d}{dt} (\mathbf{N} \boldsymbol{\alpha}) = \mathbf{M} \boldsymbol{\alpha}, \quad (3.11)$$

with the unknown vector  $\boldsymbol{\alpha} = (\alpha_1(t), \alpha_2(t), \dots)^T$ , matrix  $\mathbf{N}$  depending only on the parameters  $(a(t), b(t), c(t))$  and matrix  $\mathbf{M}$  depending on  $(a(t), b(t), c(t))$ ,  $\mathbf{q}$  and  $\boldsymbol{\Omega}^{\mathcal{B}}(t)$  in the body reference frame. System (3.11) is written in canonical form as the non-autonomous dynamical system

$$\frac{d\boldsymbol{\alpha}}{dt} = \mathbf{N}^{-1} \left( \mathbf{M} - \frac{d\mathbf{N}}{dt} \right) \boldsymbol{\alpha} = \mathcal{J} \boldsymbol{\alpha}, \quad (3.12)$$

where  $\mathcal{J}$  is the Jacobian matrix of the system. Note that in general the Jacobian matrix is not a normal matrix, i.e. it does not commute with its complex conjugate  $\mathcal{J} \mathcal{J}^\dagger \neq \mathcal{J}^\dagger \mathcal{J}$ . Because of the difficulty to build the basis elements of  $\mathcal{V}_n$  and the Jacobian  $\mathcal{J}$  for an arbitrary forcing, previous global studies have only considered low degree polynomials  $n \leq 6$  (Kerswell 1993; Lebovitz & Lifschitz 1996a; Wu & Roberts 2011; Vantieghem *et al.* 2015; Barker 2016; Barker *et al.* 2016).

The stability of basic flow (2.2) is governed by the system (3.12). We determine the stability in one of the following ways. If the Jacobian  $\mathcal{J}$  is steady, then system (3.12) reduces to the eigenvalue problem

$$\lambda_i \boldsymbol{\alpha}_i = \mathcal{J} \boldsymbol{\alpha}_i, \quad (3.13)$$

with  $\lambda_i = \sigma_i + i\omega_i$  the  $i$ -th eigenvalue. If  $\mathcal{J}$  is periodic of period  $T$ , then we perform a Floquet stability analysis. We seek solutions of the form  $\{\mathbf{p}_i(t) \exp(\mu_i t)\}$ , where  $\{\mathbf{p}_i(t)\}$  are functions of period  $T$  and  $\{\mu_i\}$  the Floquet exponents. The latter are the eigenvalues of the monodromy matrix  $\boldsymbol{\Phi}(T)$  at time  $T$ , defined by the problem

$$\frac{d\boldsymbol{\Phi}}{dt} = \mathcal{J} \boldsymbol{\Phi}, \quad \boldsymbol{\Phi}(0) = \mathbf{I}, \quad (3.14)$$

with  $\mathbf{I}$  the identity matrix. The growth rate  $\sigma_i$  and the frequency  $\omega_i$  of the  $i$ -th Floquet mode are

$$\sigma_i = \frac{1}{T} \Re_e [\ln(\mu_i)] \quad \omega_i = \frac{1}{T} \Im_m [\ln(\mu_i)], \quad (3.15)$$

The growth rate of the most dangerous unstable flow for both eigen and Floquet solvers is  $\sigma = \max_i \sigma_i$  and its associated frequency is  $\omega$ .

Finally if the Jacobian  $\mathcal{J}$  has an arbitrary time dependence, then we solve the system (3.12) as an initial-value problem. The basic flow is unstable if at least one component of the state vector has an exponential growth, i.e.  $\alpha_i(t) \propto \exp(\sigma_i t)$  with  $\sigma_i > 0$ . In practice, to determine the growth rate  $\sigma$  we fit

$$\ln \left( \sum_i |\alpha_i(t)| \right) \propto \sigma t. \quad (3.16)$$

To reduce the source of uncertainties, we start fitting the law (3.16) when the amplitude of  $\sum_i |\alpha_i(t)|$  is large enough compared to its initial value.

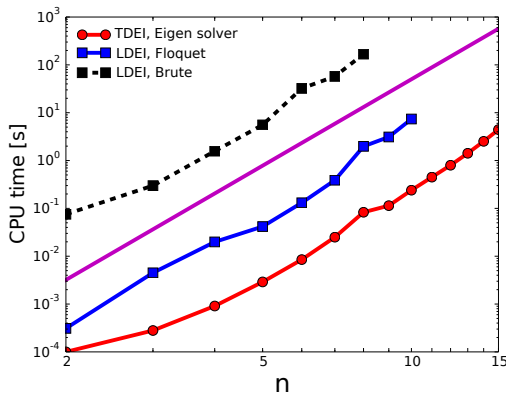


FIGURE 2. Characteristic CPU time to compute a growth rate for tidally-driven and libration-driven instabilities presented below in section 4 with the different numerical solvers. To smooth out the variability of computation time between different parameters, we compute a stability map of 100 points in the plane  $(\beta_{ac}, \Omega_0)$  for tides and in the plane  $(\beta_0, 2e)$  for longitudinal-libration to extract an average time for one iteration. Circle symbols stand for tidal forcing and square ones for longitudinal libration. Dashed lines shows eigenvalue or Floquet solvers and solid lines brute-force solver. The magenta solid line shows the power law  $\propto n^6$ , in good agreement with the numerical scaling.

### 3.3. Numerical implementation

The matrix  $\mathbf{N}$ , its time derivative and the matrix  $\mathbf{M}$  are first computed symbolically with Sympy (<http://www.sympy.org/>), a computer algebra system (CAS) for Python, which is used to manipulate the Cartesian polynomials  $x^i y^j z^k$  in a symbolic way. Then we convert them to Fortran subroutines with the Sympy fcode function and finally we wrap them with f2py (Peterson 2009) for fast numerical evaluation inside Python using Numpy (Van Der Walt *et al.* 2011). The Jacobian  $\mathcal{J}$  is computed numerically, because we cannot compute the symbolic inverse  $\mathbf{N}^{-1}$  for arbitrary  $n$ . As time solver we use an explicit Runge-Kutta solvers with adaptive step-size and dense output (available in the Python library Scipy). Performing a survey in parameter space is an embarrassingly parallel problem, and our implementation takes full advantage of this situation using mpi4py (<http://mpi4py.scipy.org/>).

To validate our implementation, we have first considered the precession of a spheroid. This benchmark is described in Appendix C, showing a perfect agreement with previous studies (Kerswell 1993; Wu & Roberts 2011). Then we assess the performance of our code in figure 2, which shows the evolution of CPU time with  $n$  for the tidally-driven and libration-driven flows considered below (see subsections 4.2 and 4.3). We compare the eigensolver for tidal flows with Floquet and time-step solvers for libration. We observe that the CPU time always scales more or less as  $n^6$ , in agreement with formula (3.4). Indeed the number of basis elements scales as  $n^3$  and so the number of elements in matrices  $\mathbf{N}$  and  $\mathbf{M}$  is of order  $n^6$ . As expected the eigenvalue solver is faster than Floquet solver, which is itself faster than the time-step solver. However the accurate pre-factors vary and are not significant, since they depend on both the numerical parameters of the chosen solver and the considered mechanical forcing.

## 4. Stability of an orbiting fluid ellipsoid

In this section, the stability of an orbiting fluid ellipsoid is considered using the method of sections 2 and 3. We first describe the model and the governing equations in §4.1.

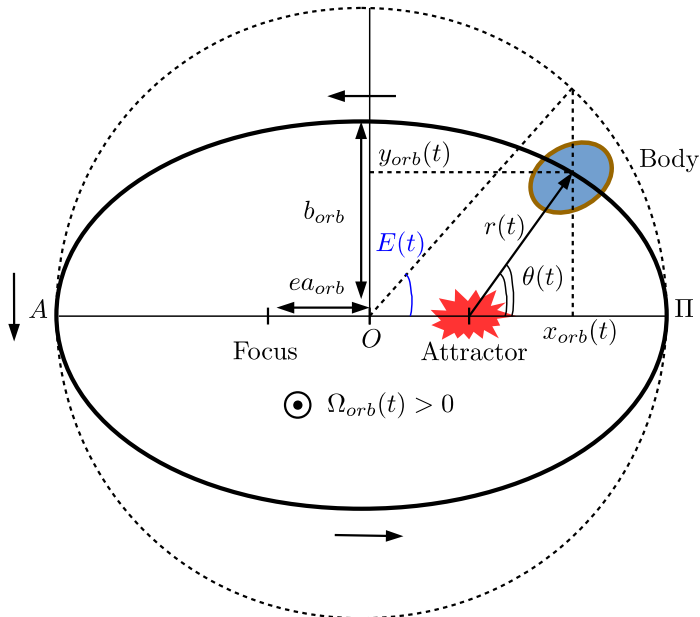


FIGURE 3. Kepler elliptical orbit for a two-body problem. The fluid body rotates around an attractor with the spin velocity  $\Omega_{orb}(t) > 0$  orthogonal to the orbital plane. The elliptical orbit (thick black line) of center  $O$  has an eccentricity  $e$ , semi-axis  $a_{orb}$  and  $b_{orb}$ , a perihelion point  $\Pi$ , a aphelion point  $A$ . Dashed black line is the circumscribed circle of radius  $a_{orb}$ . The position vector of the orbiting body from the attractor center of mass is  $r(t)$ . We denote the true anomaly  $\theta(t)$  and the mean anomaly  $E(t)$  the angle with respect to the auxiliary circle (outer dashed line). Using Cartesian coordinates centered on the attractor (at a focus of the orbit), the position of the orbiting body is  $x_{orb} = a_{orb}(\cos E - e)$  and  $y_{orb} = a_{orb}\sqrt{1 - e^2} \sin E$ .

Then, we evaluate the performance of our method by revisiting two particular cases of this general problem: the circular orbit (§4.2) and the case of synchronized bodies on weakly elliptical orbits (§4.3). Finally, we solve for the stability of a fluid ellipsoid moving along a Kepler orbit in §4.4. In this case, time variations of the ellipsoidal axis can play a significant role and drive vigorous instabilities.

#### 4.1. Modeling of orbitally-driven flows

We study the stability of a fluid ellipsoid of mass  $m$  orbiting on an elliptical orbit of eccentricity  $e$  around an attractor of mass  $M$ . For simplicity, we do not consider the general forcing described in section 2, which requires to solve numerically the vorticity equation (2.4) to find the (nonlinear) basic flow (2.2). Instead we assume a null obliquity such that the rotation vectors are along  $\hat{z}$ , i.e.  $\boldsymbol{\Omega}^W(t) = \Omega_w(t) \hat{z}$  and  $\boldsymbol{\Omega}^B(t) = \Omega_b(t) \hat{z}$ . We write the fluid spin rate  $\Omega_w(t)$  in dimensionless form as

$$\Omega_w(t) = 1 + \delta\Omega_w(t), \quad (4.1)$$

such that it has a steady unitary component and periodic length-of-day variations  $\delta\Omega_w(t)$ . We also consider that the tidal bulge always points towards the attractor (instantaneous bulge response), i.e.  $\Omega_b(t) = \Omega_{orb}(t)$  with  $\Omega_{orb}(t)$  the orbital rotation rate of the body along  $\hat{z}$ .

With our mechanical forcing we can solve analytically equation (2.4) in the limit of vanishing viscosity ( $E^{1/2} \rightarrow 0$ ). In the permanent regime, the basic flow (2.2) has the

same symmetry as the forcing, i.e.

$$q_x = q_y = 0. \quad (4.2)$$

The vorticity equation (2.4) then reduces to its vertical component

$$\frac{dq_z}{dt} + \frac{d\Omega_{orb}}{dt} = E^{1/2}\lambda_r [q_z - \Omega_w(t) + \Omega_{orb}(t)]. \quad (4.3)$$

In the limit of vanishing viscosity ( $E^{1/2} \rightarrow 0$ ), the homogeneous solution of (4.3) vanishes and the particular solution gives the solution in the permanent regime

$$q_z = 1 - \Omega_{orb}(t). \quad (4.4)$$

It shows that the periodic length-of-day variations  $\delta\Omega_w(t)$  do not play any role in the limit of vanishing viscosity, since in equation (4.3)  $\Omega_w(t)$  only appears in the viscous term. Hence, the basic flow (2.2) reduces to

$$\mathbf{U} = [1 - \Omega_{orb}(t)](-[1 + \beta_{ab}(t)]y\hat{\mathbf{x}} + [1 - \beta_{ab}(t)]x\hat{\mathbf{y}}), \quad (4.5)$$

where we introduce the (time-dependent) equatorial ellipticity

$$\beta_{ab}(t) = \frac{|a^2 - b^2|}{a^2 + b^2} < 1. \quad (4.6)$$

In the literature, the stability of basic flows (4.5) has only been studied when  $\beta_{ab}$  is constant. We relax this assumption in section 4.4.

The time dependencies of  $\Omega_{orb}(t)$  and  $\beta_{ab}(t)$  are given by the orbital dynamics. The physical problem is sketched in figure 3. We introduce the orbital period  $T$  and  $\Omega_0 = 2\pi/T$  the mean orbiting rate of the body along the elliptical orbit. The orbit is characterized by its mean orbital semi-axes  $(a_{orb}, b_{orb})$ . Following Murray & Dermott (1999), an elliptical orbit is described by Kepler's equation at a given time  $t$ ,

$$E(t) - e \sin E(t) = \Omega_0 t, \quad (4.7)$$

with  $E(t)$  the eccentric anomaly. The orbital rotation rate on the elliptical orbit is

$$\Omega_{orb}(t) = \frac{d\theta}{dt} = \Omega_0 \frac{(1 + e \cos \theta(t))^2}{(1 - e^2)^{3/2}}. \quad (4.8)$$

where  $\theta(t)$  is the true anomaly defined by

$$\theta(t) = 2 \arctan \left[ \sqrt{\frac{1+e}{1-e}} \tan \left( \frac{E(t)}{2} \right) \right]. \quad (4.9)$$

The distance  $r(t)$  between the body and its attractor is

$$r(t) = a_{orb} \frac{1 - e^2}{1 + e \cos \theta(t)} = a_{orb} (1 - e \cos E(t)). \quad (4.10)$$

Then we estimate at first order the equatorial ellipticity (4.6) of the fluid ellipsoid with an hydrostatic balance. Following (Cébron *et al.* 2012a) it gives

$$\beta_{ab}(t) = \frac{3}{2}(1 + k_2) \frac{M}{m} \left( \frac{D}{r(t)} \right)^3 = \beta_0 \left( \frac{1 + e \cos \theta(t)}{1 - e^2} \right)^3 < 1, \quad (4.11)$$

with  $\beta_0$  a characteristic equatorial ellipticity,  $D$  the mean spherical radius of the fluid ellipsoid of mass  $m$ ,  $M$  the mass of the attractor and  $k_2$  the potential Love number. The latter can be computed with the Clairaut-Radau theory (e.g. Van Hoolst *et al.* 2008).

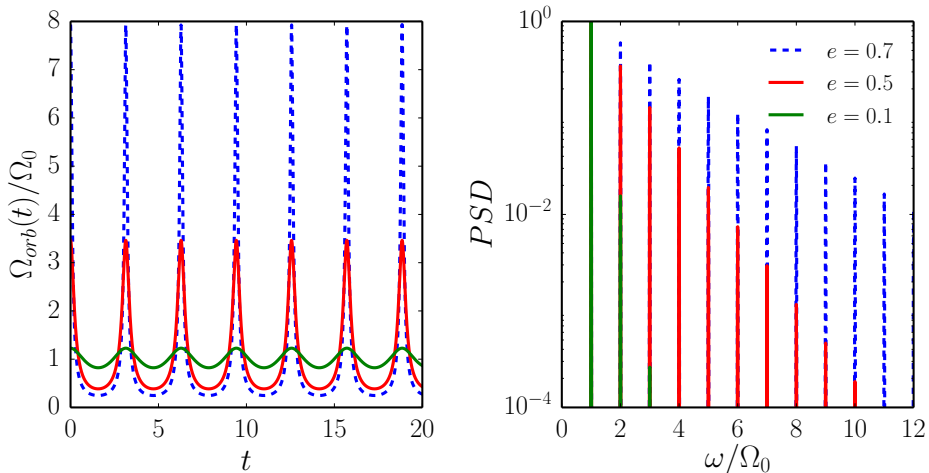


FIGURE 4. (Left) Normalized orbital spin rate  $\Omega_{orb}(t)/\Omega_0$  given by formula (4.8) for various eccentricities  $e$ . Kepler’s equation (4.7) is solved with an iterative Newton’s algorithm at each time step. (Right) Associated power spectrum density (PSD) in function of the normalized frequency  $\omega/\Omega_0$  of the Fourier transform.

Note that  $\beta_0$  is the ellipticity of a body of same mass  $m$  but on a circular orbit ( $e = 0$ ) of radius  $a_{orb}$  (dashed circle in figure 3). However it is not the averaged value in time of  $\beta_{ab}(t)$ . The ellipticity  $\beta_0$  refers to the static (tidal) bulge or equilibrium tide (Zahn 1966). The fluctuations in time superimposed on this equilibrium tide are the dynamical tides (Zahn 1975), which are excited by the periodic terms of the tidal potential. From formula (4.11), the dynamical tides lead to a minimum value of ellipticity  $\beta_{\min} = \beta_0(1 + e)^{-3}$  at the aphelion point  $A$  ( $\theta = \pi$ ) and a maximum  $\beta_{\max} = \beta_0(1 - e)^{-3}$  at the perihelion point  $I$  ( $\theta = 0$ ). Because  $\beta_{ab}(t) < 1$ , the maximum eccentricity  $e_{\max}$  for a given ellipticity  $\beta_0$  is

$$e_{\max} = 1 - \beta_0^{1/3}. \quad (4.12)$$

Finally to take into account all the possible triaxial geometries we introduce the polar ellipticity  $\beta_{ac}(t) = (a^2 - c^2)/(a^2 + c^2)$ . The limit  $\beta_{ac} \rightarrow 1$  corresponds to the limit case of a disk ( $c = 0$ ), whereas  $\beta_{ac} \rightarrow -1$  corresponds to an infinite cylinder ( $c \rightarrow \infty$ ).

For a circular orbit ( $e = 0$ ) the orbital rotation rate is steady  $\Omega_{orb}(t) = \Omega_0$  and  $\beta_{ab}(t) = \beta_0$ . For an elliptical orbit ( $e \neq 0$ ), we determine  $\Omega_{orb}(t)$  by solving Kepler’s equation (4.7) numerically using an iterative Newton’s algorithm (starting with  $E = 0$  as initial guess at  $t = 0$ ). We show in figure 4 the normalized ratio  $\Omega_{orb}(t)/\Omega_0$  and its associated power spectrum density for different eccentricities.  $\Omega_{orb}(t)$  has a fundamental period  $T = 2\pi/\Omega_0$  but, as  $e$  is increased, more and more harmonics are required to properly describe  $\Omega_{orb}(t)$ .

Finally it is worth noting that the case  $\Omega_0 = 1$  corresponds to a synchronized body, since the dimensional averaged orbital rate and the averaged fluid spin rate are equal. When  $\Omega_0 \neq 1$  the body is not synchronized, there is a mean differential rotation between the elliptical deformation and the fluid spin rate over one spin period.

#### 4.2. Tidally-driven elliptical instability on a circular orbit ( $e = 0$ )

In this subsection we focus on the effect of the equilibrium tide on a circular orbit ( $e = 0$ ). The fluid ellipsoid has steady semi-axes  $(a, b, c)$  and rotates at the steady orbital

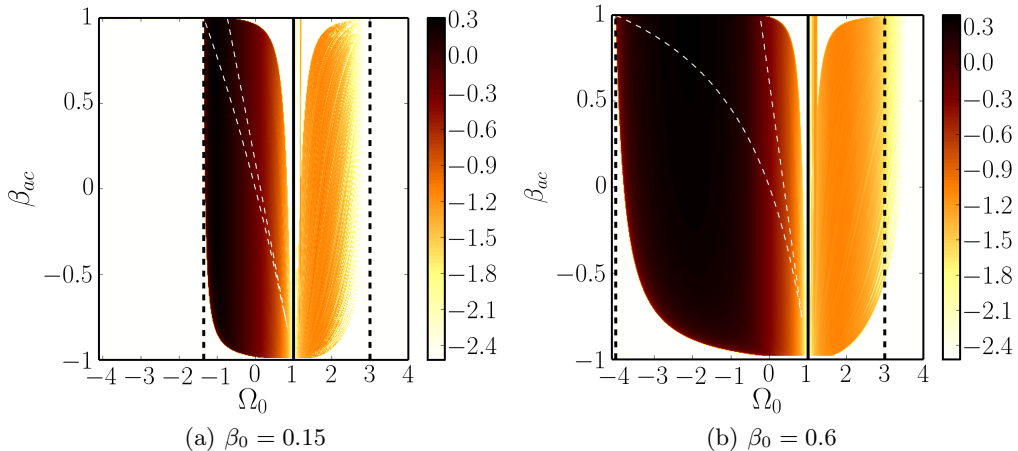


FIGURE 5. (a) & (b) Areas of instability of the tidally-driven flow in the  $(\beta_{ac}, \Omega_0)$  plane at degree  $n = 15$ . Colormap shows  $\log_{10}(\sigma/\beta_0)$ . White areas correspond to marginally stable regions. Triaxial geometry  $a = \sqrt{1 + \beta_0}$  and  $b = \sqrt{1 - \beta_0}$  and  $c = a\sqrt{(1 - \beta_{ac})/(1 + \beta_{ac})}$ . Vertical dashed black lines represent the lower and upper bounds of the forbidden zone  $\text{FZ}_{\beta_0}$ . The solid black line indicates the synchronized case  $\Omega_0 = 1$  (no instability). White dashed lines correspond to  $\sigma/\beta_0 = 0.01$  for the stability problem reduced to degree  $n = 1$ , such that the spin-over instability is excited in between (in this case,  $\sigma$  is analytically known, see e.g. Roberts & Wu 2011).

rate  $\Omega_0$ . Basic flow (4.5) thus reduces to the tidally-driven basic flow

$$\mathbf{U} = (1 - \Omega_0) [-(1 + \beta_0)y \hat{\mathbf{x}} + (1 - \beta_0)x \hat{\mathbf{y}}]. \quad (4.13)$$

This flow is unstable if  $\Omega_0 \neq 1$ , leading to the so-called tidally-driven elliptical instability (TDEI).

On one hand, TDEI has been widely studied with a local (WKB) analysis in unbounded domains assuming perturbations of small wavelengths (Bayly 1986; Craik 1989; Waleffe 1990; Cébron *et al.* 2012a). Using first-order expansion in  $\beta_0$ , Le Dizès (2000) shows that the TDEI exists in the range  $(\beta_0 + 1)/(\beta_0 - 1) \leq \Omega_0 \leq 3$ . Outside this range, the flow is stable and lies in the so-called forbidden zone for finite  $\beta_0$ , hereafter denoted  $\text{FZ}_{\beta_0}$ . The local growth rate  $\sigma_{\text{wkb}}$  is at leading order (equation 32 of Le Dizès 2000)

$$\frac{\sigma_{\text{wkb}}}{|1 - \Omega_0|} = \max_{\theta_0} \frac{1}{4} \sqrt{(1 + \cos \theta_0)^4 \beta_0^2 - 4 \left[ 2 - 4 \left( 1 + \tilde{\Omega}_0 \right) \cos \theta_0 \right]^2} + \mathcal{O}(\beta_0^2), \quad (4.14)$$

with  $\tilde{\Omega}_0 = \Omega_0/(1 - \Omega_0)$  and  $\theta_0$  the colatitude angle between the vertical axis  $\hat{\mathbf{z}}$  and the local wave vector of the plane-wave perturbation, ranging in  $[0, \pi]$ . Angle  $\theta_0$  is chosen to maximize  $\sigma$ . In the limit  $\beta_0 \rightarrow 0$ , the elliptical instability only exists for  $-1 \leq \Omega_0 \leq 3$ . Outside this range, the flow lies in the forbidden zone of the TDEI for  $\beta_0 \rightarrow 0$ , hereafter denoted  $\text{FZ}_0$ . In this limit, the growth rate (4.14) reduces to the formula devised by Craik (1989)

$$\frac{\sigma_{\text{wkb}}}{|1 - \Omega_0|} = \frac{(3 + 2\tilde{\Omega}_0)^2}{16(1 + \tilde{\Omega}_0)^2} \beta_0, \quad (4.15)$$

for  $\cos \theta_0 = 1/[2(1 + \tilde{\Omega}_0)]$  which maximizes  $\sigma$ . Finally in the range  $(\beta_0 + 1)/(\beta_0 - 1) \leq \Omega_0 \leq -1$ , which lies in  $\text{FZ}_0$ , formula (4.14) gives a non-zero growth rate of (equation 44

of Le Dizès 2000)

$$\frac{\sigma_{\text{wkb}}}{|1 - \Omega_0|} = \sqrt{\beta_0^2 - 4(\tilde{\Omega}_0 + 1/2)^2} \quad (4.16)$$

for  $\theta_0 = 0$ . When  $\Omega_0 \geq 3$ , formula (4.14) gives  $\sigma_{\text{wkb}} = 0$ , such that there is no TDEI predicted by the local analysis (at this order in  $\beta_0$ ).

On the other hand, global stability analysis of tidal basic flow (4.13) has been mainly performed for weakly deformed spheroids (Lacaze *et al.* 2004) or cylinders (Malkus 1989; Eloy *et al.* 2003). Triaxial ellipsoids have been considered (Gledzer & Ponomarev 1978, 1992; Kerswell 2002; Roberts & Wu 2011; Barker *et al.* 2016; Barker 2016), but only allowing perturbations of small polynomial degrees ( $n \leq 6$ ). Such large-wavelength instabilities do not compare well with the afore-mentioned local stability analysis.

Using our framework, we can reach much larger polynomial degrees  $n$ . Global stability results at  $n = 15$  are shown in figure 5, where the ratio  $\sigma/\beta_0$  of the instability is computed for two equatorial ellipticities ( $\beta_0 = 0.15$  and  $\beta_0 = 0.6$ ). We always find  $\sigma = 0$  when  $\Omega_0 = 1$ , as expected. When  $\beta_0$  increases, the zone of instability extends but lies in the forbidden zone  $\text{FZ}_{\beta_0}$  with an exception for the largest  $\beta_0$ . Indeed we find that TDEI is excited when  $\Omega_0 \geq 3$ , which is unexpected. It is due to detuning effects not taken into account in the local analysis. We observe that ellipsoids spinning in the retrograde direction ( $\Omega_0 < 0$ ) are more unstable than the prograde ones ( $\Omega_0 > 0$ ). By varying the polynomial degree, we observe that TDEI for prograde rotation ( $\Omega_0 > 0$ ) appears at larger  $n$  than TDEI for retrograde rotation ( $\Omega_0 < 0$ ). As an example the so-called spin-over mode (Kerswell 2002), associated with the linear basis ( $n = 1$ ), appears only for  $\Omega_0 < 0$ . Similarly the most unstable  $\sigma$  is mainly reached at smaller  $n$  for retrograde rotation than for prograde rotation (not shown). Finally we observe an effect of  $\beta_{ac}$  at large values of  $|\beta_{ac}|$ . There, higher polynomial degrees are probably needed to properly describe the instabilities.

In figure 6 we show the most dangerous unstable flows of the TDEI, at various  $\Omega_0$  for  $\beta_0 = 0.15$ . Note that the spatial structures of flows, at the same value of  $\Omega_0$  but at  $\beta_0 = 0.6$ , are similar (not shown). In all these flows, the motion seems to be concentrated in conical layers forming an angle  $\alpha$  with the rotation axis. High intensity surface flows arise where the surface has this same angle (or equivalently where the surface is perpendicular to the local wave vector). Between these layers, the flow has low or zero amplitude. Some flows also exhibit one or several nodes in azimuth.

In figure 6 (a) obtained at  $\Omega_0 = -1$ , the flow has the structure of a stack of pancake (SoP), a structure already observed in experiments (Grannan *et al.* 2014), direct simulations (Favier *et al.* 2015) and theory (Barker *et al.* 2016). In this instability, each pancake moves horizontally in the direction opposite to its neighbours, in a plane at  $45^\circ$  from the main equatorial axes where the stretching is maximum (Waleffe 1990). It is illustrated by the streamlines in figure 7. This unstable mode is stationary (zero frequency). High amplitudes are located near the poles. Note also that the number of pancakes in this unstable mode increases as  $n$  increases, as suggested by figure 7. However this number seems to be insensitive to the amplitude of the equilibrium tide  $\beta_0$  and to  $\beta_{ac}$  (not shown). Such a small-scale flow will undoubtedly lead to turbulence if it reaches high-enough amplitudes.

In contrast, at  $\Omega_0 = -0.5$  the unstable flow shown in figure 6(b) for  $n = 15$  is the same for  $n = 10$  and  $n = 6$ . It is mostly an equatorially symmetric mode dominated by an  $m = 1$  azimuthal symmetry. High intensities are found on the rotation axis and within a surface band at mid-latitudes.

At  $\Omega_0 = -0.1$ , the flow has 6 azimuthal zeros, no energy on the rotation axis and a

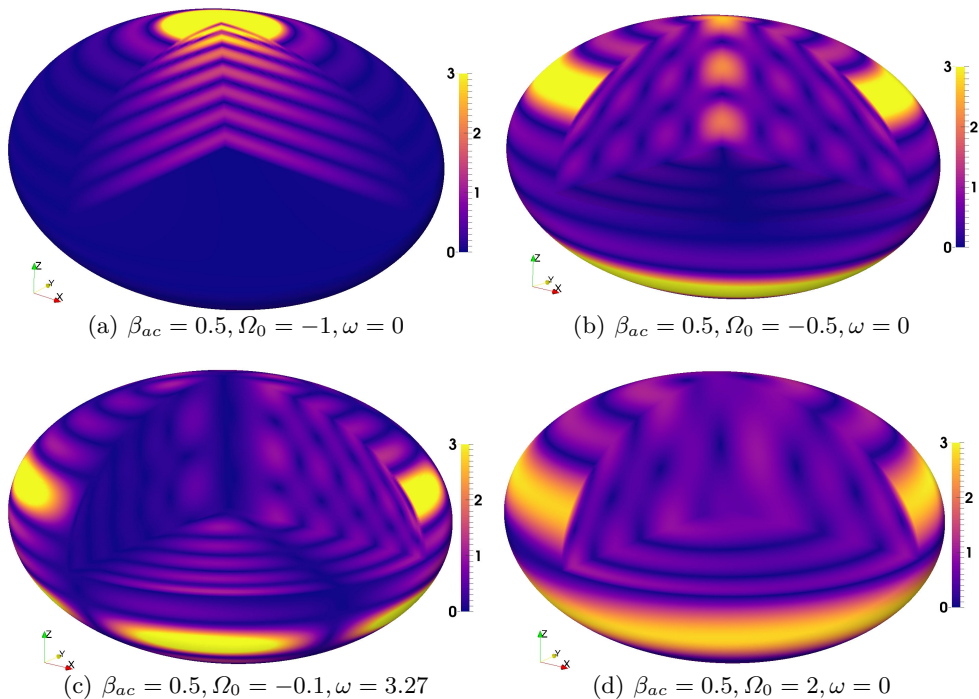


FIGURE 6. 3D renderings of the most unstable flows associated with figure 5. Degree  $n = 15$  and amplitude of equilibrium tide  $\beta_0 = 0.15$ . Velocity magnitude  $\|\mathbf{u}\|$  is shown in meridional/equatorial planes and at the ellipsoidal surface. The colormap is saturated for  $\|\mathbf{u}\| \geq 3$ .

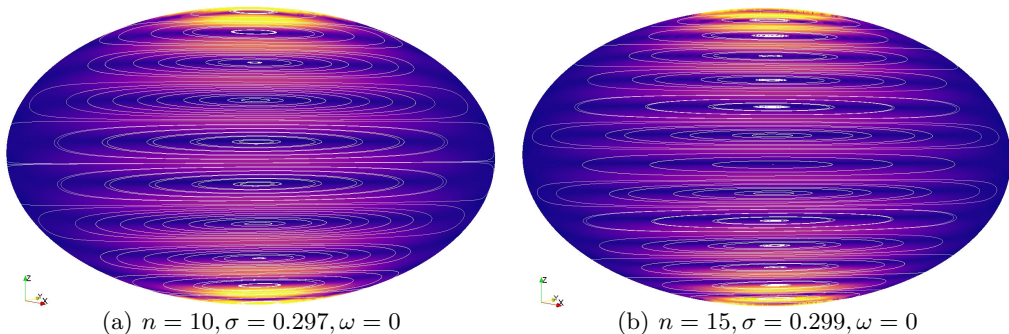


FIGURE 7. "Stack of pancakes"-like instability for  $\beta_0 = 0.15, \beta_{ac} = 0.5$  and  $\Omega_0 = -1$ . Magnitude  $\|\mathbf{u}\|$  and velocity streamlines in the meridional plane at 45 degrees from the long axis where the stretching is maximum.

high intensity band at mid-latitude close to the surface. We obtain a similar structure at larger scale at  $\Omega_0 = 2$ .

In figure 8 we quantitatively compare the growth rate from the local formula (4.14) with our global results at a high degree ( $n = 20$ ). At  $\beta_0 = 0.15$ , the agreement is striking. We note however that for  $\Omega_0 < -1$  and  $\beta_{ac} < 0$ , our global stability analysis yields lower growth rates than the local analysis, especially at large  $\beta_0$ . Similarly, the global analysis indicates stable flows near  $\Omega_0 = 1$  for  $\beta_{ac} > 0$ , especially at small  $\beta_0$ , whereas both global

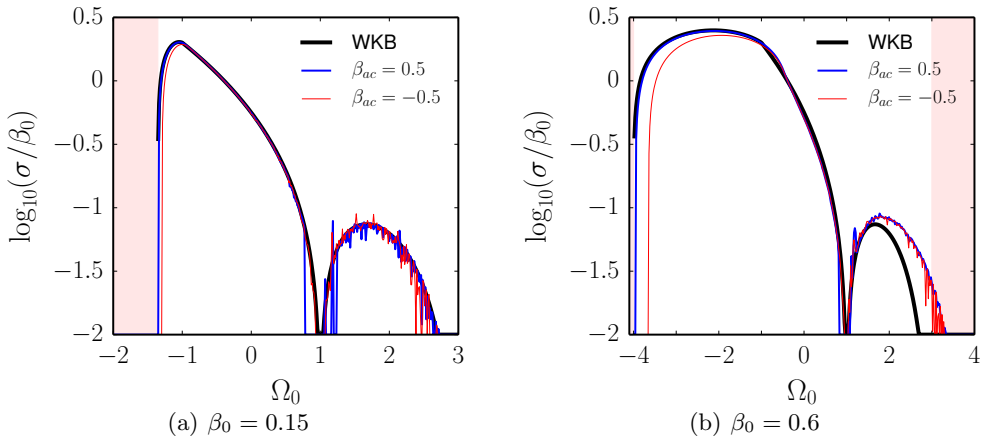


FIGURE 8. Growth rate of the TDEI obtained by local theory (4.14) and our global stability analysis at degree  $n = 20$ . Shaded areas are stable regions for the local theory. These curves correspond to cuts in the maps of figure 5.

analysis at  $\beta_{ac} < 0$  and the local analysis indicate unstable flows. We also observe that for large values of  $\beta_0$ , the flows for  $\Omega_0 > 1$  are more unstable than what is predicted by local theory, and that TDEI can even exist when  $\Omega_0 \geq 3$ , a region that is stable in the local theory.

However, the local analysis of Le Dizès (2000) given by formula (4.14) does predict that the TDEI at finite  $\beta_0$  extends well beyond the region that is unstable at  $\beta_0 \ll 1$ , that is  $-1 \leq \Omega_0 \leq 3$ . Larger values of  $\beta_0$  allow more unstable couplings. This coupling effect of  $\beta_0$  is highlighted in figure 9, with good matching between local and global results. Note that this very same effect has recently been put forward by Barker (2016), as shown in Appendix D.

#### 4.3. Libration-driven elliptical instability on weakly elliptical orbit ( $0 < e \ll 1$ )

We investigate here the stability of a synchronized fluid body on an orbit of small eccentricity  $0 < e \ll 1$ . The associated forcing, called longitudinal librations, can give birth to the libration-driven elliptical instability (LDEI). We distinguish the following two limit cases of longitudinal librations.

If the rigidity of the container is strong enough, the entire body rigidly rotates with a fixed shape. Dynamical tides are neglected with respect to the equilibrium tide such that  $\beta_{ab}(t) = \beta_0$ . The forcing bears the name of physical librations. A differential rotation exists between the fluid spin rate and the equilibrium tide, rotating at leading order at

$$\Omega_{orb}(t) = 1 + \epsilon \sin(t), \quad (4.17)$$

with  $\epsilon \leq 2e$  the libration amplitude. This amplitude depends on the rheology of the celestial body. LDEI driven by physical librations has been studied amongst others by Cébron *et al.* (2012b); Noir *et al.* (2012); Grannan *et al.* (2014) and Favier *et al.* (2015). Note that physical librations (4.17) may contain multiple frequencies due to the presence of several attracting bodies (Rambaux & Williams 2011). In the limit  $\beta_0 \ll 1$ , the local growth rate of this physical LDEI is (Cébron *et al.* 2012b)

$$\sigma_{wkb} = \frac{17}{64} \epsilon \beta_0. \quad (4.18)$$

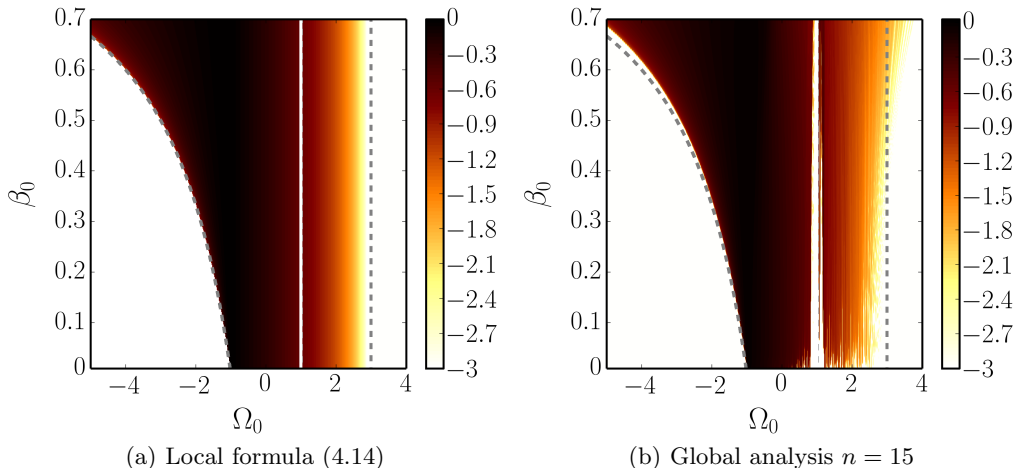


FIGURE 9. Areas of instability of the tidally-driven flow in the  $(\beta_0, \Omega_0)$  plane. Colormap shows  $\log_{10}(\sigma/[\beta_0|1 - \Omega_0|])$ . Triaxial geometry  $a = \sqrt{1 + \beta_0}$ ,  $b = \sqrt{1 - \beta_0}$  and  $c = 1/(ab)$  such that the triaxial container has a constant dimensionless volume  $4\pi/3$ . On the vertical white line  $\Omega_0 = 1$  the TDEI does not exist. Black dashed lines  $\Omega_0 = (1 + \beta_0)/(1 - \beta_0)$  and  $\Omega_0 = 3$  are the bounds of the forbidden zone  $\text{FZ}_{\beta_0}$  corresponding to formula (4.14).

According to the local formula (4.18) LDEI is triggered for any non-zero  $\epsilon$  and  $\beta_0$ .

On the other hand, if the rigidity of the container is zero, then the ellipsoidal cavity always points toward the attractor and the container has a time-dependent ellipticity. A differential rotation exists between the fluid spin rate and the dynamical tides (superimposed on the equilibrium tide). We expand (4.8) and (4.11) at first order in  $e$  to obtain

$$\Omega_{orb}(t) = 1 + 2e \cos t, \quad (4.19)$$

$$\beta_{ab}(t) = \beta_0(1 + 3e \cos t). \quad (4.20)$$

In the inviscid framework of this work, we call this forcing optical librations (because optical librations amplitude is  $2e$ , see e.g. Murray & Dermott 1999). However, note that this forcing simply associates a prescribed time-evolution of  $(a, b, c)$  to the forcing (4.17), rather than considering a constant ellipsoidal shape. At this order, the time dependence of the dynamical tide is monochromatic, in agreement with numerical results of figure 4 at small  $e$ . Physical librations with maximum amplitude  $\epsilon = 2e$  are recovered if we neglect the dynamical tides (4.20), yielding  $\beta_{ab}(t) = \beta_0$ .

We compare in figure 10 physical libration (a) with optical librations (b), assuming a libration amplitude  $\epsilon = 2e$  in the physical case. We fix the polynomial degree  $n = 5$  to capture only the large-scale unstable flows. Flows of higher degrees are not essential for this comparison. We show the ratio  $\sigma/\sigma_{\text{wkb}}$  to compare global results and local formula (4.18). The global growth rates of physical librations do not reach yet the local growth rates, as expected for  $n = 5$ . For very small eccentricities  $e$ , predictions for physical and optical librations are in broad agreement. However for larger amplitudes optical librations drive more violent instabilities than physical librations. The growth rates are much larger and can even be higher than those predicted by formula (4.18), clearly enhancing the LDEI. Thus, with the same libration amplitude, physical librations underestimate the growth rate predicted by optical librations for large eccentricities. Dynamical tides drive instabilities and cannot be neglected in the dynamics of bodies on eccentric Kepler orbit.

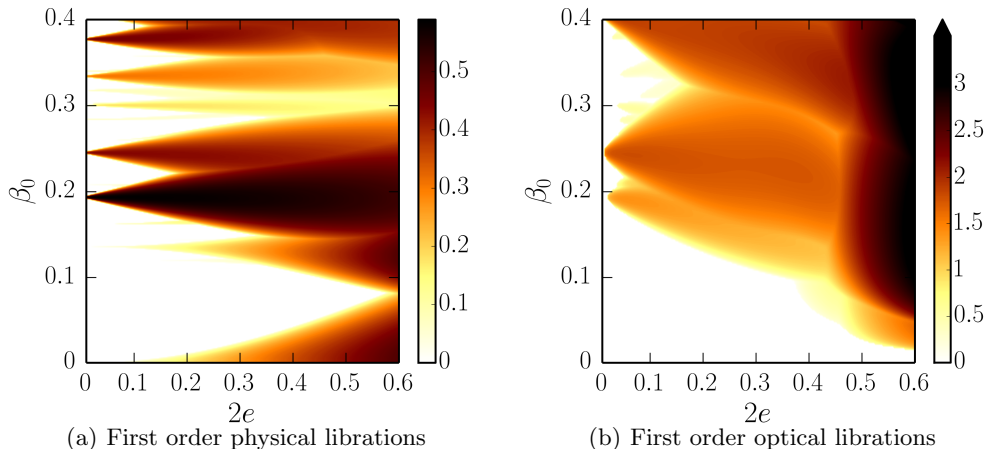


FIGURE 10. Survey of the libration-driven elliptical instability for physical librations (4.17) and optical librations (4.19) in the plane  $(\beta_0, 2e)$ . Polynomial degree  $n = 5$ . Colormap shows ratio  $\sigma/\sigma_{\text{wkb}}$  with  $\sigma_{\text{wkb}}$  given by formula (4.18). White areas correspond to marginally stable regions. Triaxial geometry  $a(t) = \sqrt{1 + \beta_{ab}(t)}$ ,  $b(t) = \sqrt{1 - \beta_{ab}(t)}$  and  $c(t) = [a(t)b(t)]^{-1}$ . (a)  $\beta_{ab}(t) = \beta_0$  and  $\epsilon = 2e$ . (b)  $\beta_{ab}(t) = \beta_0(1 + 3e \cos t)$ . Growth rates  $\sigma/\beta_0 \leq 0.01$  are filtered out because we chose an integration time not long enough.

Furthermore, we checked that this phenomenon is reinforced by taking into account the next orders of  $\beta_{ab}(t)$  and  $\Omega_{\text{orb}}(t)$ . Consequently, we turn to the general orbitally-driven elliptical instability.

#### 4.4. General orbitally-driven elliptical instability (ODEI)

We consider here the general case of a fluid ellipsoid orbiting on a Kepler orbit of eccentricity  $0 \leq e < 1$ . We numerically solve the full governing equations described in section 4.1. We consider here only oblate containers ( $a \geq b \geq c$ ), which are typically the shapes of celestial bodies. Moreover, we consider ellipsoids of constant dimensionless volume  $4\pi/3$ , with semi-axes length

$$a = R\sqrt{1 + \beta_{ab}(t)}, \quad b = R\sqrt{1 - \beta_{ab}(t)} \quad \text{and} \quad c = 1/(ab). \quad (4.21)$$

The equatorial ellipticity  $\beta_{ab}(t)$  is given by formula (4.11) and  $R$  is a free parameter governing the polar ellipticity  $\beta_{ac}(t)$  of the ellipsoid. The oblateness condition  $b \geq c$  at each time leads to the sufficient condition  $R \geq R_m$ , with

$$R_m = [(1 - \beta_{\text{max}}^2)(1 - \beta_{\text{max}})]^{-1/6} \quad (4.22)$$

and  $\beta_{\text{max}} = \beta_0(1 - e)^{-3}$  the maximum value of  $\beta_{ab}(t)$  along the orbit.

It is important to recall that, when the full equations are solved, the forcing contains a lot of frequencies. In a planetary context, multiple harmonics are always present, which challenges theoretical predictions. Here, we show that our framework can handle this additional complexity, at the expense of a larger computational cost.

In figure 11 we survey the stability of orbitally-driven flow (4.5) in the parameter space  $(\Omega_0, e)$  for  $\beta_0 = 0.05$  and  $\beta_0 = 0.3$ . TDEI considered in subsection 4.2 corresponds to the horizontal line  $e = 0$ , where instabilities are predicted for  $(1 + \beta_0)/(\beta_0 - 1) \leq \Omega_0 \leq 3$  by the local theory. The LDEI considered in subsection 4.3 corresponds to the vertical line  $\Omega_0 = 1$  ( $e \ll 1$ ), and instabilities are thus also expected for  $\Omega_0 = 1$  (whereas TDEI is

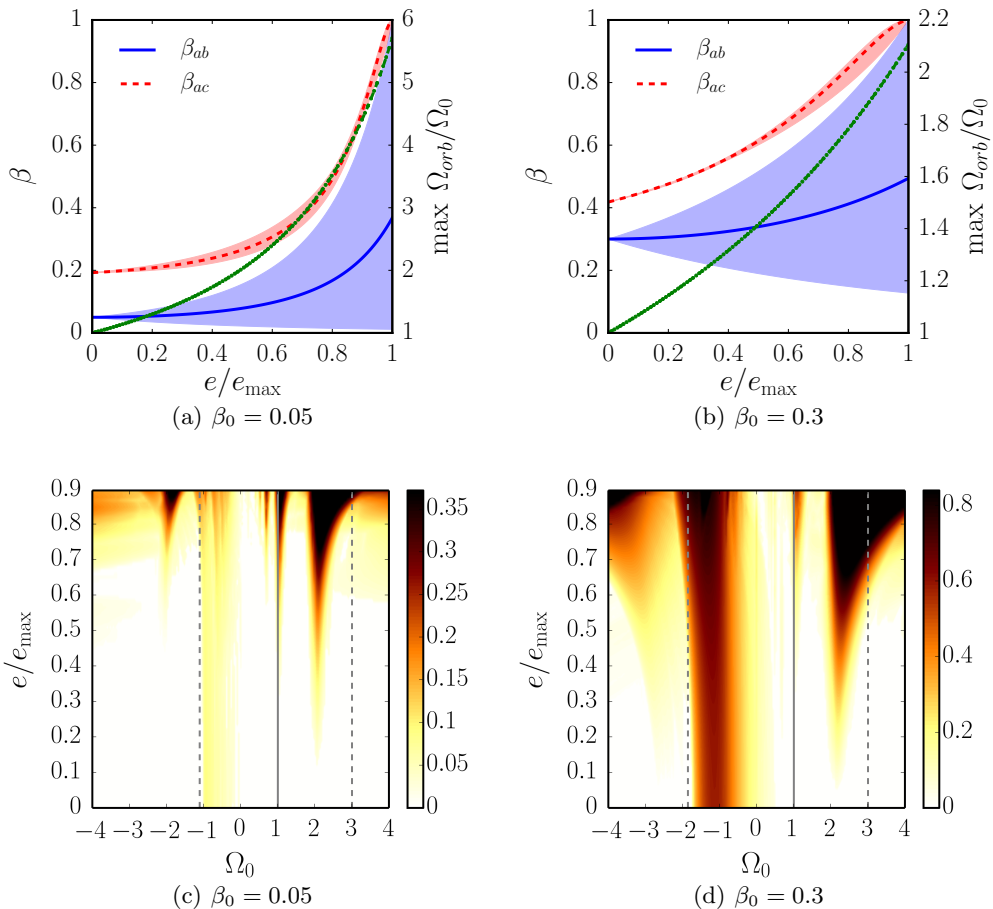


FIGURE 11. Orbitally-driven elliptical instability. (a) & (b) Range of values of  $\beta_{ab}$  (blue) and  $\beta_{ac}$  (red) for an orbit of eccentricity  $e/e_{\max}$  considered. Blue thick (resp. red dashed) line shows the mean value of  $\beta_{ab}$  (resp.  $\beta_{ac}$ ) along the orbit. Second vertical axis shows the maximum of ratio  $\Omega_{orb}/\Omega_0$  (green dotted line) for various normalized eccentricities  $e/e_{\max}$ . (c) & (d) Survey of the instability of the orbitally-driven flow (eq. 4.5) in the plane  $(e/e_{\max}, \Omega_0)$  for degree  $n = 6$ . Colormap shows the growth rate  $\sigma$ , saturated for  $\sigma \geq 0.4 \sigma_{\max}$ . White areas correspond to marginally stable regions. The containers considered are oblate with  $R = R_m + 0.05$ . Vertical black line corresponds to the synchronized case ( $\Omega_0 = 1$ ) driving the LDEI (see §4.3). The horizontal line  $e = 0$  corresponds to the TDEI (see §4.2). Vertical dashed black lines are the bounds of the forbidden zone  $FZ_{\beta_0}$  of the TDEI valid for  $e = 0$  and  $\beta_{ab} = \beta_0$ .

expected for  $\Omega_0 \neq 1$ ). We notice the effect of finite deformations, which gives instabilities for  $\Omega_0 \leq -1$ .

Interestingly, our survey uncovers a strong new instability around  $\Omega_0 = 2$ , i.e. when the fluid spin period is twice the orbital period. Figure 12 compares the growth rate of the TDEI (circular orbit) to the one of the ODEI for a Kepler orbit of finite eccentricity. For  $(\beta_0 + 1)/(\beta_0 - 1) \leq \Omega_0 \leq 1$ , the growth rate of the ODEI has almost the same value as for the TDEI. Furthermore, the flows associated to ODEI at  $\Omega_0 = -1, -0.49$  and  $-0.1$  in figure 13 (b) to (d) are similar to the ones associated to TDEI in figure 6 (a) to (c), although not computed at the same  $n$ . Around  $\Omega_0 = 1$  we see the peak corresponding to LDEI. The corresponding flow is displayed in figure 13.

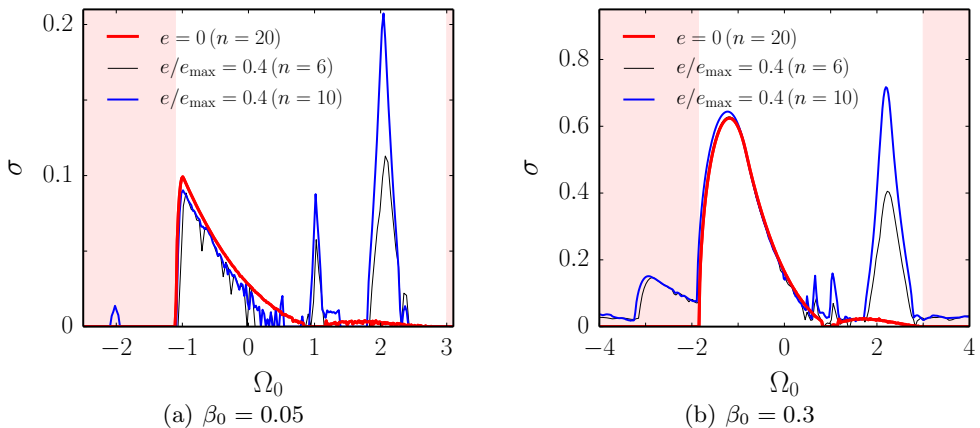


FIGURE 12. Growth rate of the orbitally-driven elliptic instability for a Kepler orbit of fixed eccentricity ( $e/e_{\max} = 0.4$ ) compared to the case of zero eccentricity (TDEI,  $e = 0$ ). Shaded areas are the forbidden zone  $FZ_{\beta_0}$  for the TDEI, valid for local perturbations at  $e = 0$ .

New instabilities driven by the non-circular Kepler orbits are also clearly visible in Figure 12, even at low  $\beta_0$ . In particular at  $\Omega_0 \simeq -2$  where a region stable with respect to the TDEI is here unstable. The flow associated with this new instability at  $\Omega_0 = -2$  is shown in figure 13 (a) and displays vertical stripes. They are similar to the stacked pancakes seen at  $\Omega_0 = -1$  but here stacked along an equatorial axis. The largest growth rate is achieved around  $\Omega_0 = 2$ , in a region already unstable for the TDEI but the ODEI leads to growth rates about ten times larger in this peak near  $\Omega_0 = 2$ . This instability is even stronger as  $n$  is increased from  $n = 6$  to  $n = 10$ , suggesting a rather small-scale instability. Indeed, the flow shown in figure 13 (f) exhibits intense motion localized in patches around the equator, and is very different from the TDEI flow at  $\Omega_0 = 2$  in figure 6 (d). We expect both the growth rate and this localization to increase as  $n$  is increased further. Finally, for the value of  $n$  considered here, we remark that at large  $\beta_0$  the basicflow is found unstable everywhere for  $-4 \leq \Omega_0 \leq 4$  and  $e/e_{\max} \gtrsim 0.4$ .

We show in figure 14 the LDEI on eccentric orbits, taking into account the exact orbital motion and associated dynamical tides. Compared to figure 10 (b) where only the first order effect of dynamical tides is taken into account, we observe in figure 14 (a) that LDEI can be more vigorous than predicted before. Indeed, the growth rates can be tens times larger than predicted by local analysis (4.18) for large eccentricities. Note that the growth rates are still increasing from  $n = 10$  to  $n = 15$ . Hence, even though we find that the basic flow is stable when  $e \ll 0.1$ , we expect it to be unstable at higher  $n$ . Similarly, we expect the growth rate of the LDEI to be even larger as higher  $n$  are considered. Interestingly, the effect of dynamical tides is more important at  $\beta_0 = 0.05$  than at  $\beta_0 = 0.3$ . In figure 14 (b) we show the most dangerous unstable flow for an equilibrium tide of amplitude  $\beta_0 = 0.05$  and an eccentricity  $e/e_{\max} = 0.4$ .

## 5. Conclusion

We have studied the global stability of uniform vorticity basic flows induced by the shape variation of ellipsoids on Kepler orbits. Although viscous effects such as the thin Ekman layers and internal shear layers (Kerswell 1995) are neglected, the considered

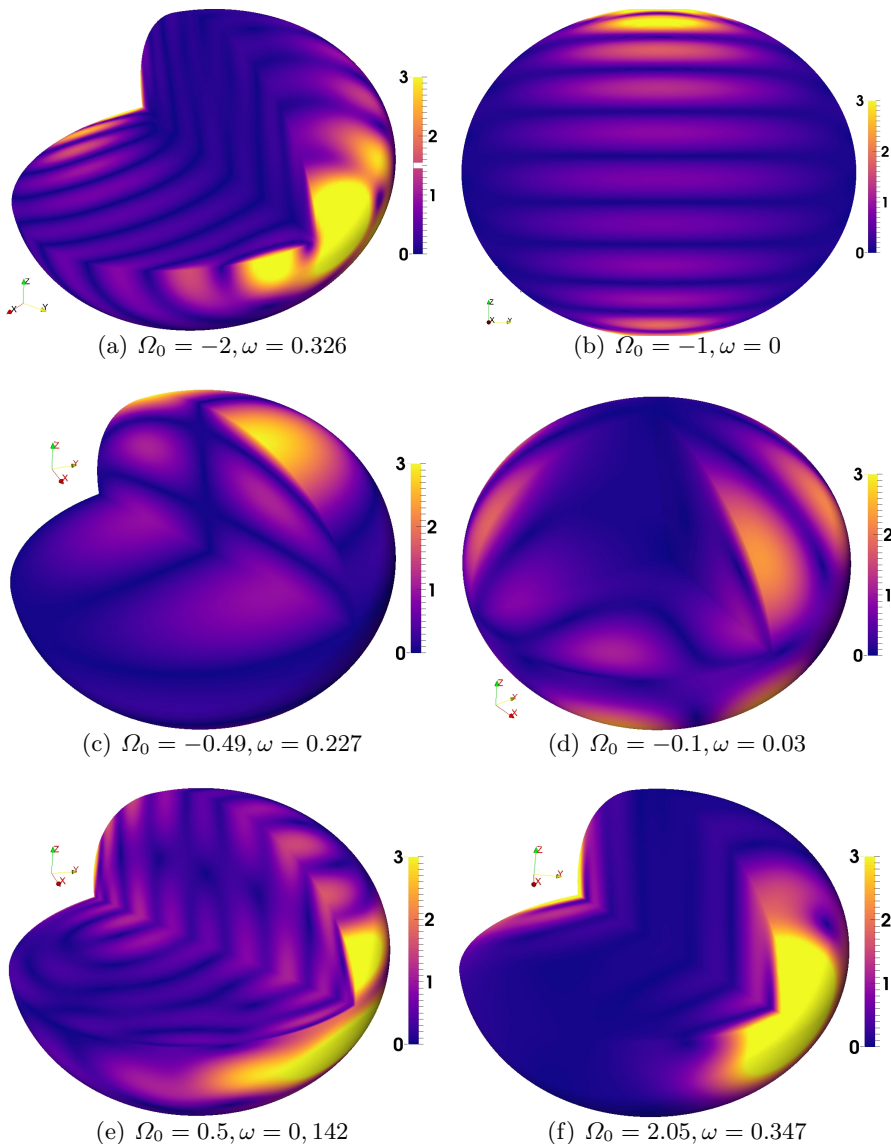


FIGURE 13. 3D renderings of the most unstable flows associated with figure 12, at  $n = 10$ ,  $e/e_{max} = 0.4$  and  $\beta_0 = 0.05$ . Velocity magnitude  $\|\mathbf{u}\|$  is shown in meridional/equatorial planes and at the ellipsoidal surface. The colormap is saturated for  $\|\mathbf{u}\| \geq 3$ . Flows are computed at  $\theta(t) = \pi/2$  on the orbit (see figure 3).

uniform vorticity basic flows are good approximations of the mechanically-driven basic flows (e.g. Busse 1968; Noir & Cébron 2013; Vantieghem *et al.* 2015).

The flow stability in ellipsoids is a long standing issue, which dates back to the stability study of self-gravitating ellipsoids. For instance, Riemann (1860) considered the stability of flows linear in space coordinates for such ellipsoids, by using linear perturbations (i.e.  $n = 1$ ). Actually, it is mainly the elliptical instability which destabilizes these so-called Riemann ellipsoids (Lebovitz & Lifschitz 1996*b*) and, surprisingly, the free surface aspect

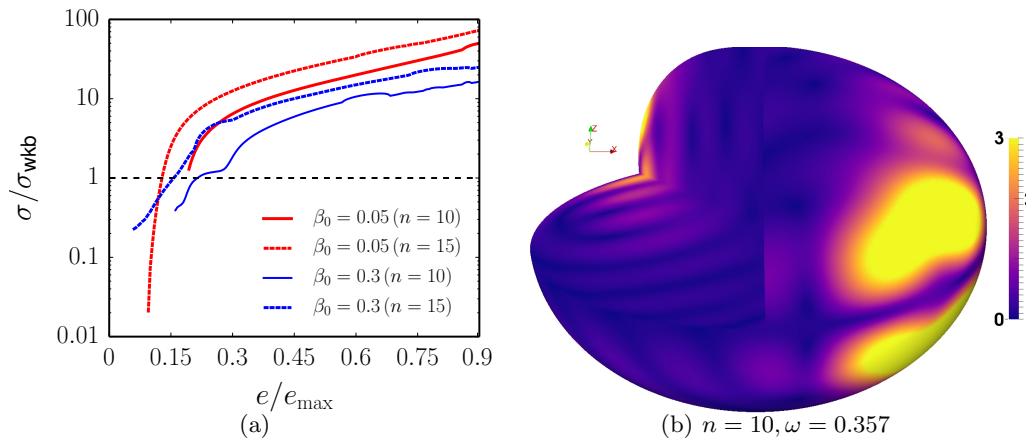


FIGURE 14. Libration-driven elliptical instability ( $\Omega_0 = 1$ ) for arbitrary Kepler orbits. (a) Ratio  $\sigma/\sigma_{\text{wkb}}$  with  $\sigma_{\text{wkb}}$  the local growth rate of LDEI given by formula (4.18). (b) Flow magnitude  $\|\mathbf{u}\|$  for  $\beta_0 = 0.05$ ,  $e/e_{\text{max}} = 0.4$ . Flow computed at  $\theta(t) = \pi/2$  on the orbit (see fig. 3).

(i.e. the surface gravity modes) does not really affect their stability (Barker *et al.* 2016). Our study of flows in rigid ellipsoids is thus relevant for this question.

We have developed a framework that combines symbolic and numerical computations. It allows to study the global stability of any self-gravitating ellipsoid, taking into account perturbations of unprecedentedly small wavelength. Indeed, our freely available Python code has been used up to polynomial degree  $n = 25$ , which corresponds to more than 6000 basis elements. Our framework also handles ellipsoidal shapes not limited to small departures from the sphere. Furthermore, two new effects due to an eccentric orbit are taken into account: a time-dependent ellipsoidal shape (dynamical tides) and the time-variation of the rotation rate of the principal body axes (or tidal bulge), both leading to a non-harmonic forcing (see figure 4).

We prove the capabilities of the method by considering the stability of a fluid ellipsoid moving on an eccentric orbit. With this challenging case we recover the limiting cases previously studied in the literature and unify them (TDEI and LDEI) into a global framework. The good agreement at low ellipticity between previous local analysis (WKB) and our global analysis confirms that the local stability computations can be applied to celestial bodies. In particular, instabilities in retrograde planets are rather insensitive to realistic orbital effects and are thus well described by the local theory of TDEI derived by Le Dizès (2000). As a consequence, the spin-over ( $n = 1$ ) is replaced by other, more complex, unstable flows with larger growth rates (see examples in figure 6).

However, we find that realistic orbital effects – the time-dependence of the ellipsoid deformation, combined with the time-dependence of the tidal bulge rotation rate – are important in several cases, leading to new instabilities. Firstly, the dynamical tides superimposed on the libration forcing ( $\Omega_0 = 1$ ) lead to much larger growth rates, as shown in figure 10 and 14. The growth rate can even exceed the one predicted by the local analysis with a fixed shape. Secondly, prograde spinning bodies exhibit a vigorous instability near the 2:1 spin-orbit resonance ( $\Omega_0 \simeq 2$ ). This new instability is a small-scale, localized one, and has higher growth rates for eccentric orbits (see figure 12). Thirdly, retrograde bodies exhibit a new instability in the stable zone of the TDEI ( $\Omega_0 < (\beta_0 + 1)/(\beta_0 - 1)$ ), as seen in figure 12.

All these findings show that dynamical tides can drive instabilities and cannot be

neglected in the dynamics of bodies on eccentric Kepler orbit. In particular, the eccentricities and tidal amplitude of some hot Jupiters may be comparable with values required for the onset of the ODEI (at high polynomial degree  $n$ ), inside and outside the forbidden zone.

This work is also a first step toward the study of viscously damped inertial instabilities in arbitrary ellipsoids. Indeed, we plan to reintroduce the viscosity as a correction, allowing direct comparisons between the theory and simulations or experiments, all performed at finite values of viscosity and deformation.

## Acknowledgments

The SIREN code developed for this study is freely available at <https://bitbucket.org/vidalje/siren>. J. V. acknowledges the French *Ministère de l'Enseignement Supérieur et de la Recherche* for his PhD grant. This work was partially funded by the French *Agence Nationale de la Recherche* under grant ANR-14-CE33-0012 (MagLune) and by the 2017 TelluS program from CNRS-INSU (PNP) AO2017-1040353. ISTerre is part of Labex OSUG@2020 (ANR10 LABX56). Most figures were produced using matplotlib (<http://matplotlib.org/>).

## Appendix A. Mechanical forcings used in the literature

Description of rotation vectors and their associated reference frames is achieved by using Euler angles, measured in the inertial frame. We express the Euler angles using the ZYZ convention, as described by Goldstein (1965). We introduce the precession angle  $\psi_w(t)$ , the nutation angle  $\alpha_w(t)$  and the proper rotation angle  $\phi_w(t)$  to define  $\boldsymbol{\Omega}^W(t)$ . Similarly, we introduce the precession angle of the orbital partner  $\psi_b(t)$ , the nutation angle of the orbital partner  $\alpha_b(t)$  and the rotation of the orbital partner  $\phi_b(t)$  to describe  $\boldsymbol{\Omega}^B(t)$ . We gather the different cases studied in the literature in table 1.

With our convention, the mantle (resp. body) rotation vector  $\boldsymbol{\Omega}^W$  (resp.  $\boldsymbol{\Omega}^B$ ) has the three components in the mantle (resp. body) frame

$$\boldsymbol{\Omega}^i(t) = \begin{pmatrix} \sin \alpha_i \cos \phi_i \, d\psi_i/dt + \sin \phi_i \, d\alpha_i/dt \\ -\sin \alpha_i \sin \phi_i \, d\psi_i/dt + \cos \phi_i \, d\alpha_i/dt \\ \cos \alpha_i \, d\psi_i/dt + d\phi_i/dt \end{pmatrix}, \quad (\text{A } 1)$$

where the index  $i$  refers to the mantle or the body frame. In equation (2.4) the mantle rotation vector has to be written in the body frame. To this end, the direction cosine matrix  $\mathbf{R}_i^I$  relating a vector of components  $\mathbf{x}_i$  in the frame  $i$  (mantle or body) and  $\mathbf{x}_I$  in the inertial frame, defined by

$$\mathbf{x}_i(t) = \mathbf{R}_i^I(t)\mathbf{x}_I(t), \quad (\text{A } 2)$$

is

$$\mathbf{R}_i^I = \begin{pmatrix} -\sin \alpha_i \sin \psi_i + \cos \alpha_i \cos \psi_i \cos \phi_i & \sin \phi_i \cos \psi_i + \sin \psi_i \cos \alpha_i \cos \phi_i & \sin \alpha_i \cos \phi_i \\ \sin \phi_i \cos \psi_i + \sin \psi_i \cos \alpha_i \cos \phi_i & -\sin \phi_i \sin \psi_i \cos \alpha_i + \cos \phi_i \cos \psi_i & -\sin \alpha_i \sin \phi_i \\ -\sin \alpha_i \cos \psi_i & -\sin \alpha_i \sin \psi_i & \cos \alpha_i \end{pmatrix}.$$

Finally, the time derivative of the body rotation vector in equation (2.4), expressed in

	Rigid containers				Deformable containers		
	LibLat	Prec. 1	LDEI 1	Prec. 2	LDEI 2	TDEI	
$\Omega^{\mathcal{W}}(t)$	$\psi_w(t)$	$t$	$\epsilon t$	0	$\epsilon t$	0	$\psi_0$
	$\alpha_w(t)$	$\frac{\epsilon}{f} \sin(ft)$	$\alpha_0$	0	$\alpha_0$	0	$\alpha_0$
	$\phi_w(t)$	0	$t$	$t + \frac{\epsilon}{f} \sin(ft)$	$t$	$t$	$t$
$\Omega^{\mathcal{B}}(t)$	$\psi_b(t)$	$t$	$\epsilon t$	0	$\epsilon t$	0	$\psi_0$
	$\alpha_b(t)$	$\frac{\epsilon}{f} \sin(ft)$	$\alpha_0$	0	$\alpha_0$	0	$\alpha_0$
	$\phi_b(t)$	0	$t$	$t + \frac{\epsilon}{f} \sin(ft)$	$\epsilon t$	$t + \frac{\epsilon}{f} \sin(ft)$	$\epsilon t$

TABLE 1. Euler angles used to describe mechanical forcings in the fluid mechanic literature (non exhaustive). The time unit is  $\Omega_s^{-1}$ . LibLat: Latitudinal libration (Vantighem *et al.* 2015), LongLib: Longitudinal libration. Prec. 1: Precession (Kerswell 1993; Wu & Roberts 2011; Noir & Cébron 2013) LDEI 1: Libration-driven elliptical instability (Wu & Roberts 2013; Cébron *et al.* 2014). Prec. 2: Precession (Cébron *et al.* 2010b), LDEI 2: Libration-driven elliptical instability (Kerswell & Malkus 1998), TDEI: Tidally-driven elliptical instability (Kerswell 2002; Cébron *et al.* 2010a).  $\epsilon$  is the dimensionless amplitude of the mechanical forcing (not necessarily small).  $f$  is the frequency of the mechanical forcing.  $\psi_0$  and  $\alpha_0$  are arbitrary constants.

the body frame, is

$$\frac{d\Omega^{\mathcal{B}}}{dt} \cdot \hat{\mathbf{x}} = \sin \alpha_b \sin \psi_b \frac{d\phi_b}{dt} \frac{d\psi_b}{dt} - \sin \alpha_b \cos \psi_b \frac{d^2 \phi_b}{dt^2} - \sin \psi_b \frac{d^2 \alpha_b}{dt^2} \quad (\text{A } 3)$$

$$- \cos \alpha_b \cos \psi_b \frac{d\alpha_b}{dt} \frac{d\phi_b}{dt} - \cos \psi_b \frac{d\alpha_b}{dt} \frac{d\psi_b}{dt}, \quad (\text{A } 4)$$

$$\frac{d\Omega^{\mathcal{B}}}{dt} \cdot \hat{\mathbf{y}} = - \sin \alpha_b \sin \psi_b \frac{d^2 \phi_b}{dt^2} - \sin \alpha_b \cos \psi_b \frac{d\phi_b}{dt} \frac{d\psi_b}{dt} - \sin \psi_b \cos \alpha_b \frac{d\alpha_b}{dt} \frac{d\phi_b}{dt} \quad (\text{A } 5)$$

$$- \sin \psi_b \frac{d\alpha_b}{dt} \frac{d\psi_b}{dt} + \cos \psi_b \frac{d^2 \alpha_b}{dt^2} \quad (\text{A } 6)$$

$$\frac{d\Omega^{\mathcal{B}}}{dt} \cdot \hat{\mathbf{z}} = - \sin \alpha_b \frac{d\alpha_b}{dt} \frac{d\phi_b}{dt} + \cos \alpha_b \frac{d^2 \phi_b}{dt^2} + \frac{d^2 \psi_b}{dt^2}. \quad (\text{A } 7)$$

where  $(\hat{\mathbf{x}}, \hat{\mathbf{y}}, \hat{\mathbf{z}})$  are the unit basis vectors in the body frame.

## Appendix B. Polynomial basis of $\mathcal{V}_n$

Recently, Wu & Roberts (2011) have proposed another algorithm to build the basis elements of  $\mathcal{V}_n$ . We outline here the method. We consider first a spherical container ( $a = b = c$ ). The vorticity field is decomposed into poloidal  $\mathcal{P}_w(\mathbf{r})$  and toroidal  $\mathcal{T}_w(\mathbf{r})$  scalars as

$$\nabla \times \mathbf{u} = \nabla \times (\mathcal{T}_w \mathbf{r}) + \nabla \times \nabla \times (\mathcal{P}_w \mathbf{r}). \quad (\text{B } 1)$$

such that it obeys to the solenoidal condition. Vorticity  $\nabla \times \mathbf{u}$  is then projected onto the finite-dimensional vector space  $\mathcal{W}_{n-1}$ , made of Cartesian homogeneous monomials  $x^i y^j z^k$  of degree  $n - 1 = i + j + k$  (Vantighem 2014). Note that an element of  $\mathcal{W}_n$  is solenoidal but does not necessarily satisfy the impermeability condition.  $\mathcal{P}_w(\mathbf{r})$  is a homogeneous polynomial of degree  $n$  while  $\mathcal{T}_w(\mathbf{r})$  is a homogeneous polynomial of degree  $n - 1$ . Similarly the velocity field  $\mathbf{u}(\mathbf{r})$  is expanded into poloidal  $\mathcal{P}_u(\mathbf{r})$  and toroidal  $\mathcal{T}_u(\mathbf{r})$  scalars as

$$\mathbf{u}(\mathbf{r}) = \nabla \times (\mathcal{T}_u \mathbf{r}) + \nabla \times \nabla \times (\mathcal{P}_u \mathbf{r}). \quad (\text{B } 2)$$

Since there is an isomorphism between vector spaces  $\mathbf{W}_{n-1}$  and  $\mathbf{V}_n$  (Vantieghem 2014), we expand  $\mathbf{u}$  onto  $\mathbf{V}_n$  such that velocity scalars are related to the vorticity scalars by

$$\mathcal{T}_u = \mathcal{P}_w \quad (\text{B3})$$

and

$$\nabla^2 \mathcal{P}_u = -\mathcal{T}_w \quad \text{with} \quad \mathcal{L}^2 \mathcal{P}_u = 0 \quad \text{at} \quad r = 1, \quad (\text{B4})$$

where  $\mathcal{L}^2$  is the angular momentum operator

$$\mathcal{L}^2 = \left( y \frac{\partial}{\partial z} - z \frac{\partial}{\partial y} \right)^2 + \left( z \frac{\partial}{\partial x} - x \frac{\partial}{\partial z} \right)^2 + \left( x \frac{\partial}{\partial y} - y \frac{\partial}{\partial x} \right)^2. \quad (\text{B5})$$

The difficult part of the above algorithm is to solve equations (B4). However any homogeneous polynomial of degree  $p$  can be decomposed into harmonic homogeneous polynomials of maximum degree  $p$ , which are spherical harmonics (Backus *et al.* 1996). So we project  $\mathcal{T}_w(\mathbf{r})$  of degree  $n-1$  onto spherical harmonics as

$$\mathcal{T}_w(\mathbf{r}) = r^{n-1} \sum_{l=1}^{n-1} \sum_{m=-l}^l t_l^m \mathcal{Y}_l^m, \quad (\text{B6})$$

where  $\mathcal{Y}_l^m$  are normalized spherical harmonics of degree  $l$  and order  $m$  and  $\{t_l^m\}$  the set of spherical harmonics coefficients. The degree  $l=0$  is omitted because of the incompressible condition. Poloidal scalar solution of (B4) is of the form

$$\mathcal{P}_u = \mathcal{P}_P + \mathcal{P}_H, \quad (\text{B7})$$

with  $\mathcal{P}_P$  a particular solution of (B4) and the general solution of the homogeneous Laplace equation  $\nabla^2 \mathcal{P}_H = 0$ . Because of expansion (B6), a particular solution of equation (B4) in spherical harmonics expansion is

$$\mathcal{P}_P(\mathbf{r}) = r^{n+1} \sum_{l=1}^{n-1} \sum_{m=-l}^l \frac{-t_l^m}{(n+2)(n+1) - l(l+1)} \mathcal{Y}_l^m. \quad (\text{B8})$$

The homogeneous solution has the general form

$$\mathcal{P}_H(\mathbf{r}) = r^{n+2} \sum_{l=1}^{n+2} \sum_{m=-l}^l p_l^m \mathcal{Y}_l^m, \quad (\text{B9})$$

where the set of coefficients  $\{p_l^m\}$  is determined by the boundary condition

$$\mathcal{L}^2 \mathcal{P}_P = -\mathcal{L}^2 \mathcal{P}_H. \quad (\text{B10})$$

Once the coefficients are known we can transform the spherical harmonics expansion back into a Cartesian form. Finally, the Poincaré transform (Poincaré 1910)

$$(x, y, z) \leftarrow \left( \frac{x}{a}, \frac{y}{b}, \frac{z}{c} \right) \quad \text{and} \quad (u_x, u_y, u_z) \leftarrow \left( \frac{u_x}{a}, \frac{u_y}{b}, \frac{u_z}{c} \right) \quad (\text{B11})$$

is used to convert the solutions valid in spheres to solutions valid in ellipsoids of axis  $(a, b, c)$ .

The implementation of Wu & Roberts (2011) relies on symbolic computations of (B6), (B8) and (B9). Basis elements up to degrees  $n=5$  are explicitly given in their Appendix A. However, their symbolic algorithm breaks down for degrees  $n > 6$ , because spherical harmonic coefficients  $t_l^m$  cannot be computed analytically for higher degrees. We have extended their method to build the basis for degrees  $n \geq 6$ . It is achieved by combining

symbolic and numerical calculus in Python. The algorithm was also parallelized to reduce the computation time. With our implementation we can reach degrees  $n \geq 6$  because spherical harmonics coefficients are only computed numerically with the open-source library SHTNS (Schaeffer 2013). The comparison between (3.5) - (3.6) and the elements obtained above shows that the two sets are equivalent, changing only by linear combinations of the basis elements.

In practice the generation of basis elements is not restricted to a particular degree but we found that the generation of symbolic matrices  $\mathbf{M}$  and  $\mathbf{N}$  becomes impractical for degrees  $n > 18$  because of high-memory usage ( $\simeq 200$  GB). Consequently we have adopted the algorithm of Lebovitz (1989) for high degrees numerical computations, reaching degrees as high as  $n = 25$  ( $\lesssim 20$  GB). The limiting factor is then the CPU time to solve the stability problem.

### Appendix C. Precessing flow in spheroidal containers

We revisit here the precession-driven instabilities in spheroidal geometry ( $a = b \neq c$ ) studied by Kerswell (1993) and Wu & Roberts (2011). We use this case as a benchmark for our global analysis. We work in the precessing frame where the vertical axis coincides with the spheroidal axis of symmetry. Using notation of table 1, we assume a precession angle  $\alpha_0 = \pi/2$ . In this frame the body rotation vector is  $\boldsymbol{\Omega}^B = \epsilon \hat{\mathbf{x}}$ , with  $\epsilon$  the dimensionless amplitude of the precession forcing (Poincaré number). The basic flow (2.2) then reduces to

$$\mathbf{U} = -y \hat{\mathbf{x}} + [x - \mu(1 + \eta)z] \hat{\mathbf{y}} + \mu y \hat{\mathbf{z}}, \quad (\text{C1})$$

with  $\eta = 1/c^2 - 1$  the polar flattening and  $\mu = 2\epsilon/\eta$  a parameter which measures the ratio of the elliptical distortion over the shearing of the streamlines.

As shown by Kerswell (1993), no instability is associated with the linear basis ( $n = 1$ ). Wu & Roberts (2011) extended the work of Kerswell (1993) by considering basis up to degree  $n = 6$ . Results for the  $n = 2$  and  $n = 6$  basis are shown in figure 15 (a)-(b), which surveys the stability of (C1) in the plane  $(\eta, \epsilon)$ . The stability maps are in perfect agreement with the previous studies. Tongues of instabilities emerge from the  $\eta$  axis. Tongues are associated with two types of instability, namely elliptical and shear instabilities (Kerswell 1993). The former have growth rates proportional to  $\epsilon^2$  and the latter to  $\epsilon$ . Showing iso-contours of  $\sigma/\epsilon$  leads to elliptical tongues which are thicker than shearing ones. When  $n$  increases, the maximum growth rate of oblate spheroids ( $\eta > 0$ ) first increases quickly and we observe that when  $n$  is large enough ( $n > 10$ ) it slows down to reach a constant value when  $n$  increases further. On the other hand prolate spheroids ( $\eta < 0$ ) have already large growth rate close to 1 for large  $\epsilon$  and the maximum value does not really evolve with  $n$ . As noticed by Wu & Roberts (2011), the progression of unstable tongues for oblate spheroids ( $\eta > 0$ ) toward the spherical case  $\eta = 0$  is quicker than for prolate spheroids ( $\eta < 0$ ) when  $n$  increases.

Global analysis using  $n = 15$  is shown in figure 15 (c). In comparison with  $n = 6$ , new tongues of instabilities appear almost everywhere, filling the map and making the identification of the nature of the instability difficult. Valleys of less unstable modes are found for prolate and oblate ellipsoids (white dashed lines).

Figure 15 (c) draws the possible existence of instabilities for the limit of very small oblateness relevant in geophysics. For instance the Earth's liquid core has a flattening of  $\eta \simeq 0.005$ . To this end we push up the degree to  $n = 25$  in figure 15 (d) and make a zoom in the geophysical range of parameter space. We observe instability for oblate spheroid of oblatenesses as small as the one of the Earth's core. The amplitude of precession  $\epsilon$  is

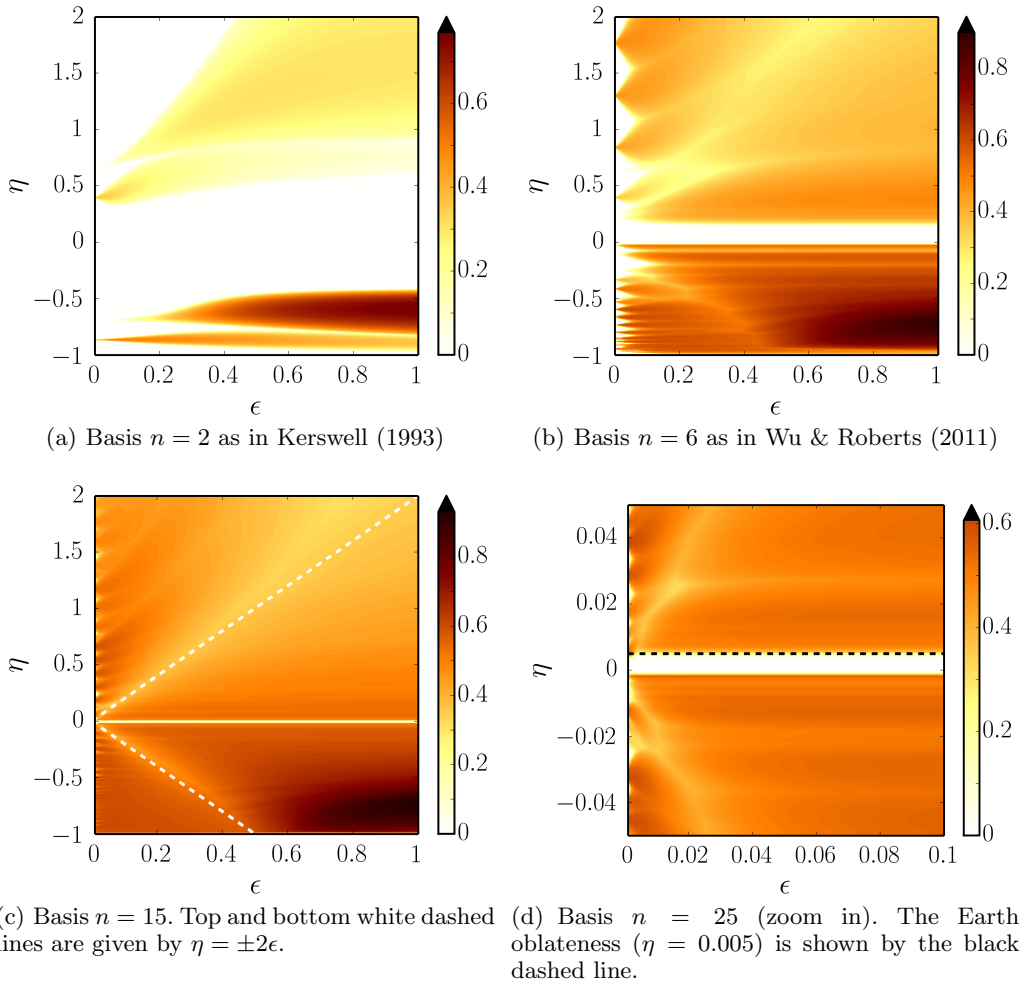


FIGURE 15. Survey of the stability of precessing basic flows (C1) in the  $(\eta, \epsilon)$  plane. Colormap shows the ratio  $\sigma/\epsilon$ . The same color scale is used for the four plots. White areas correspond to marginally stable regions.

still rather large to be consistent with geophysical values ( $\epsilon \simeq 10^{-7}$ ), but it is likely that an unstable area appears for smaller  $\epsilon$  when  $n$  is further increased.

#### Appendix D. Tidally-driven elliptical instability ( $e = 0$ ) in figures of equilibrium

We consider here a self-gravitating fluid domain on a circular orbit ( $e = 0$ ) but  $(a, b, c)$  are no longer independent of  $\Omega_0$  (as opposed to subsection 4.2). Barker *et al.* (2016) and Barker (2016) have recently considered this particular case of TDEI, considering figures of equilibrium where the equilibrium tide is related to  $\Omega_0$ . To compare our results with theirs, we choose the inverse of the dynamical frequency  $\omega_d^{-1}$  as time unit, with  $\omega_d = (4\pi G\rho/3)^{1/2}$  and  $G$  the gravitational constant. We introduce two new dimensionless parameters, namely the fluid spin rate  $\Omega_s^* = \Omega_s/\omega_G$  and the orbital spin rate  $\Omega_0^* = \Omega_s^*\Omega_0$  (note that  $\Omega_0$  is dimensionless).

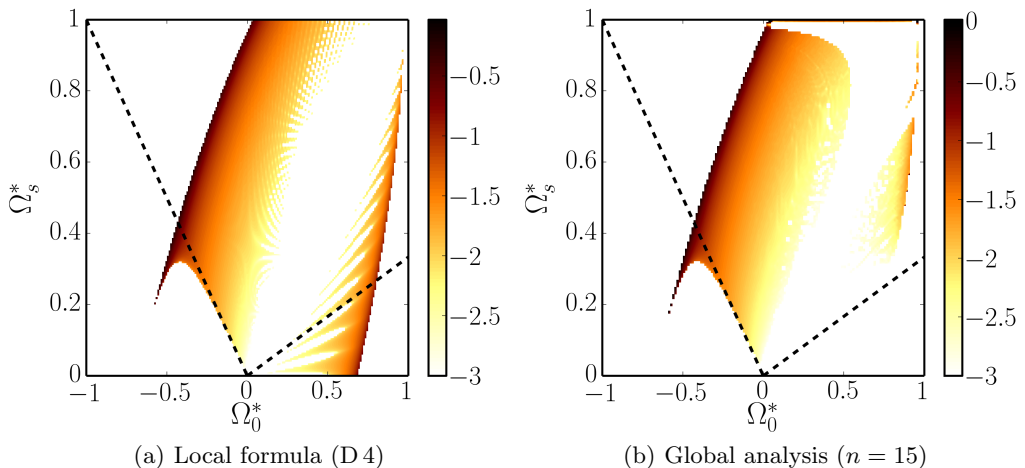


FIGURE 16. Survey of the parameter space  $(\Omega_s^*, \Omega_0^*)$  for the elliptical instability as studied by Barker (2016); Barker *et al.* (2016). Colormap shows  $\log_{10}(\sigma)$  and is saturated for ratio smaller than  $10^{-3}$ . White areas correspond to undefined ellipsoidal figures of equilibrium such that  $\beta_0 \leq 0$  or  $\beta_0 \geq 1$ . Tidal amplitude  $A = 0.025$ . The elliptical instability in the limit  $\beta_0 \ll 1$  ( Craik 1989) is obtained above the dashed black lines for  $\Omega_0^* \in [-\Omega_s^*, 3\Omega_s^*]$ .

Denoting  $A$  the tidal amplitude, Barker (2016) shows that

$$\beta_0 = \frac{3A}{2[1 - \gamma^2 - (\Omega_0^*)^2] - A} \quad (\text{D } 1)$$

with  $\gamma = \Omega_s^* - \Omega_0^*$  the differential rotation. The fluid ellipsoid semi-axes are  $a = \sqrt{1 + \beta_0}$ ,  $b = \sqrt{1 - \beta_0}$  and

$$c^2 = \frac{2[(2A + \gamma^2 + (\Omega_0^*)^2 - 1)(A - \gamma^2 - (\Omega_0^*)^2 + 1) + f]}{(A + 1)[A + 2(\gamma^2 + (\Omega_0^*)^2 - 1)]}, \quad (\text{D } 2)$$

with

$$f = 2\gamma\Omega_0^* \sqrt{[1 - 2A - \gamma^2 - (\Omega_0^*)^2][1 + A - \gamma^2 - (\Omega_0^*)^2]}. \quad (\text{D } 3)$$

They found that instabilities in ellipsoids with rigid boundaries are quantitatively similar to the ones in ellipsoids with realistic free surface deformations. Consequently the results obtained with rigid boundaries can also be applied to stellar configurations. They also report a violent instability (called "stack of pancakes"-type instability) for negative  $\Omega_0^*$ , if the tidal amplitude is sufficiently large and located outside of the unstable range  $-\Omega_s^* \leq \Omega_0^* \leq 3\Omega_s^*$  of the elliptical instability (Craik 1989). In fact, this instability is already highlighted by Le Dizès (2000) as an effect of finite  $\beta_0$  (see discussion in §4.2).

The local formula (4.14) of Le Dizès (2000) can be written in the appropriate dimensionless form

$$\frac{\sigma}{|\gamma|} = \max_{\theta_0} \frac{1}{4} \sqrt{(1 + \cos \theta_0)^4 \beta_0^2 - 4 \left[ 2 - 4 \left( 1 + \frac{\Omega_0^*}{\gamma} \right) \cos \theta_0 \right]^2} + \mathcal{O}(\beta_0^2). \quad (\text{D } 4)$$

In figure 16, we compare the global analysis at degree  $n = 15$  and the local formula (D 4). The agreement between the two approaches is very good (except near  $\Omega_s^* \geq 0.95$ ).

- ÅKERVIK, E., BRANDT, L., HENNINGSON, D. S., HEPPFNER, J., MARXEN, O. & SCHLATTER, P. 2006 Steady solutions of the Navier-Stokes equations by selective frequency damping. *Physics of Fluids* **18** (6), 068102.
- BACKUS, G., PARKER, R. L. & CONSTABLE, C. 1996 *Foundations of Geomagnetism*. Cambridge University Press.
- BARKER, A. J. 2016 Non-linear tides in a homogeneous rotating planet or star: global simulations of the elliptical instability. *Monthly Notices of the Royal Astronomical Society* **459** (1), 939–956.
- BARKER, A. J., BRAVINER, H. J. & OGILVIE, G. I. 2016 Non-linear tides in a homogeneous rotating planet or star: global modes and elliptical instability. *Monthly Notices of the Royal Astronomical Society* **459** (1), 924–938.
- BARKER, A. J. & LITHWICK, Y. 2013 Non-linear evolution of the elliptical instability in the presence of weak magnetic fields. *Monthly Notices of the Royal Astronomical Society* p. stt1884.
- BAYLY, B. J. 1986 Three-dimensional instability of elliptical flow. *Physical Review Letters* **57** (17), 2160.
- BONDI, H. & LYTTLETON, R. A. 1953 On the dynamical theory of the rotation of the Earth. II. The effect of precession on the motion of the liquid core. In *Mathematical Proceedings of the Cambridge Philosophical Society*, , vol. 49, pp. 498–515. Cambridge University Press.
- BUSSE, F. H. 1968 Steady fluid flow in a precessing spheroidal shell. *Journal of Fluid Mechanics* **33** (04), 739–751.
- CÉBRON, D. & HOLLERBACH, R. 2014 Tidally driven dynamos in a rotating sphere. *The Astrophysical Journal Letters* **789** (1), L25.
- CÉBRON, D., LE BARS, M., LEONTINI, J., MAUBERT, P. & LE GAL, P. 2010a A systematic numerical study of the tidal instability in a rotating triaxial ellipsoid. *Physics of the Earth and Planetary Interiors* **182** (1), 119–128.
- CÉBRON, D., LE BARS, M. & MEUNIER, P. 2010b Tilt-over mode in a precessing triaxial ellipsoid. *Physics of Fluids* **22** (11), 116601.
- CÉBRON, D., LE BARS, M., MOUTOU, C. & LE GAL, P. 2012a Elliptical instability in terrestrial planets and moons. *Astronomy & Astrophysics* **539**, A78.
- CÉBRON, D., LE BARS, M., NOIR, J. & AURNOU, J. M. 2012b Libration driven elliptical instability. *Physics of Fluids* **24** (6), 061703.
- CÉBRON, D., VANTIEGHEM, S. & HERREMAN, W. 2014 Libration-driven multipolar instabilities. *Journal of Fluid Mechanics* **739**, 502–543.
- CRAIK, A. D. D. 1989 The stability of unbounded two- and three-dimensional flows subject to body forces: some exact solutions. *Journal of Fluid Mechanics* **198**, 275–292.
- DASSIOS, G. 2012 *Ellipsoidal Harmonics: Theory and Applications*. Cambridge University Press.
- DEHANT, V. & MATHEWS, P. M. 2015 *Precession, Nutation and Wobble of the Earth*. Cambridge University Press.
- ELOY, C., LE GAL, P. & LE DIZÈS, S. 2003 Elliptic and triangular instabilities in rotating cylinders. *Journal of Fluid Mechanics* **476**, 357–388.
- FAVIER, B., GRANNAN, A. M., LE BARS, M. & AURNOU, J. M. 2015 Generation and maintenance of bulk turbulence by libration-driven elliptical instability. *Physics of Fluids* **27** (6), 066601.
- GLEDZER, E. B. & PONOMAREV, V. M. 1978 Finite-dimensional approximation of the motions of an incompressible fluid in an ellipsoidal cavity. *Akademiia Nauk SSSR Fizika Atmosfery i Okeana* **13**, 820–827.
- GLEDZER, E. B. & PONOMAREV, V. M. 1992 Instability of bounded flows with elliptical streamlines. *Journal of Fluid Mechanics* **240**, 1–30.
- GOEPFERT, O. & TILGNER, A. 2016 Dynamos in precessing cubes. *New J. Phys* **18**, 103019.
- GOLDSTEIN, H. 1965 *Classical Mechanics*. Pearson Education India.
- GRANNAN, A. M., FAVIER, B., LE BARS, M. & AURNOU, J. M. 2016 Tidally-forced turbulence in planetary interiors. *Geophysical Journal International* p. ggw479.
- GRANNAN, A. M., LE BARS, M., CÉBRON, D. & AURNOU, J. M. 2014 Experimental study of global-scale turbulence in a librating ellipsoid. *Physics of Fluids* **26** (12), 126601.
- HOUGH, S. S. 1895 The oscillations of a rotating ellipsoidal shell containing fluid. *Philosophical Transactions of the Royal Society of London*. A pp. 469–506.

- KERSWELL, R. R. 1993 The instability of precessing flow. *Geophysical & Astrophysical Fluid Dynamics* **72** (1-4), 107–144.
- KERSWELL, R. R. 1995 On the internal shear layers spawned by the critical regions in oscillatory Ekman boundary layers. *Journal of Fluid Mechanics* **298**, 311–325.
- KERSWELL, R. R. 1996 Upper bounds on the energy dissipation in turbulent precession. *Journal of Fluid Mechanics* **321**, 335–370.
- KERSWELL, R. R. 2002 Elliptical instability. *Annual review of fluid mechanics* **34** (1), 83–113.
- KERSWELL, R. R. & MALKUS, W. V. R. 1998 Tidal instability as the source for Io's magnetic signature. *Geophysical research letters* **25** (5), 603–606.
- KOPAL, Z. 1966 *An introduction to the study of the Moon*. Springer.
- LACAZE, L., LE GAL, P. & LE DIZÈS, S. 2004 Elliptical instability in a rotating spheroid. *Journal of Fluid Mechanics* **505**, 1–22.
- LE BARS, M., CÉBRON, D. & LE GAL, P. 2015 Flows driven by libration, precession, and tides. *Annual Review of Fluid Mechanics* **47**, 163–193.
- LE BARS, M., LACAZE, L., LE DIZÈS, S., LE GAL, P. & RIEUTORD, M. 2010 Tidal instability in stellar and planetary binary systems. *Physics of the Earth and Planetary Interiors* **178** (1), 48–55.
- LE DIZÈS, S. 2000 Three-dimensional instability of a multipolar vortex in a rotating flow. *Physics of Fluids* **12** (11), 2762–2774.
- LEBOVITZ, N. R. 1989 The stability equations for rotating, inviscid fluids: Galerkin methods and orthogonal bases. *Geophysical & Astrophysical Fluid Dynamics* **46** (4), 221–243.
- LEBOVITZ, N. R. & LIFSCHITZ, A. 1996a New global instabilities of the Riemann ellipsoids. *The Astrophysical Journal* **458**, 699.
- LEBOVITZ, N. R. & LIFSCHITZ, A. 1996b Short-wavelength instabilities of Riemann ellipsoids. *Philosophical Transactions of the Royal Society of London. Series A: Mathematical, Physical and Engineering Sciences* **354** (1709), 927.
- LORENZANI, S. & TILGNER, A. 2001 Fluid instabilities in precessing spheroidal cavities. *Journal of Fluid Mechanics* **447**, 111–128.
- MALKUS, W. V. R. 1963 Precessional torques as the cause of geomagnetism. *Journal of Geophysical Research* **68** (10), 2871–2886.
- MALKUS, W. V. R. 1968 Precession of the Earth as the cause of geomagnetism. *Science* **160** (3825), 259–264.
- MALKUS, W. V. R. 1989 An experimental study of global instabilities due to the tidal (elliptical) distortion of a rotating elastic cylinder. *Geophysical & Astrophysical Fluid Dynamics* **48** (1-3), 123–134.
- MURRAY, C. D. & DERMOTT, S. F. 1999 *Solar System Dynamics*. Cambridge University Press.
- NOIR, J., CARDIN, P., JAULT, D. & MASSON, J.-P. 2003 Experimental evidence of non-linear resonance effects between retrograde precession and the tilt-over mode within a spheroid. *Geophysical Journal International* **154** (2), 407–416.
- NOIR, J. & CÉBRON, D. 2013 Precession-driven flows in non-axisymmetric ellipsoids. *Journal of Fluid Mechanics* **737**, 412–439.
- NOIR, J., CÉBRON, D., LE BARS, M., SAURET, A. & AURNOU, J. M. 2012 Experimental study of libration-driven zonal flows in non-axisymmetric containers. *Physics of the Earth and Planetary Interiors* **204**, 1–10.
- PAIS, M. A. & LE MOUËL, J.-L. 2001 Precession-induced flows in liquid-filled containers and in the Earth's core. *Geophysical Journal International* **144** (3), 539–554.
- PETERSON, P. 2009 F2PY: a tool for connecting Fortran and Python programs. *International Journal of Computational Science and Engineering* **4** (4), 296–305.
- POINCARÉ, H. 1910 Sur la précession des corps déformables. *Bulletin Astronomique, Serie I* **27**, 321–356.
- RAMBAUX, N. & WILLIAMS, J. G. 2011 The Moon's physical librations and determination of their free modes. *Celestial Mechanics and Dynamical Astronomy* **109** (1), 85–100.
- RIEMANN, B. 1860 Untersuchungen uber die bewegung eines flussigen gleich-artigen ellipsoides. *Abh. d. Konigl. Gesell. der Wiss. zu Gottingen* **9**, 3–36.
- ROBERTS, P. H. & STEWARTSON, K. 1965 On the motion of a liquid in a spheroidal cavity of a precessing rigid body. II. *Mathematical Proceedings of the Cambridge Philosophical Society* **61** (01), 279–288.

- ROBERTS, P. H. & WU, C.-C. 2011 On flows having constant vorticity. *Physica D: Nonlinear Phenomena* **240** (20), 1615–1628.
- SCHAEFFER, N. 2013 Efficient spherical harmonic transforms aimed at pseudospectral numerical simulations. *Geochemistry, Geophysics, Geosystems* **14** (3), 751–758.
- SLOUDSKY, T. 1895 *De la rotation de la Terre supposée fluide à son intérieur*.
- STEWARTSON, K. & ROBERTS, P. H. 1963 On the motion of liquid in a spheroidal cavity of a precessing rigid body. *Journal of Fluid Mechanics* **17** (01), 1–20.
- THEOFILIS, V. 2011 Global linear instability. *Annual Review of Fluid Mechanics* **43**, 319–352.
- TILGNER, A. 2005 Precession driven dynamos. *Physics of Fluids* **17** (3), 034104.
- TILGNER, A. 2007 Kinematic dynamos with precession driven flow in a sphere. *Geophysical and Astrophysical Fluid Dynamics* **101** (1), 1–9.
- TILGNER, A. 2015 Rotational dynamics of the core. *Treatise on Geophysics* **8**, 183–212.
- VAN DER WALT, S., COLBERT, S. C. & VAROQUAUX, G. 2011 The NumPy array: a structure for efficient numerical computation. *Computing in Science & Engineering* **13** (2), 22–30.
- VAN HOOLST, T., RAMBAUX, N., KARATEKIN, Ö., DEHANT, V. & RIVOLDINI, A. 2008 The librations, shape, and icy shell of Europa. *Icarus* **195** (1), 386–399.
- VANTIEGHEM, S. 2014 Inertial modes in a rotating triaxial ellipsoid. *Proceedings of the Royal Society A: Mathematical, Physical and Engineering Science* **470** (2168), 20140093.
- VANTIEGHEM, S., CÉBRON, D. & NOIR, J. 2015 Latitudinal libration driven flows in triaxial ellipsoids. *Journal of Fluid Mechanics* **771**, 193–228.
- WALEFFE, F. 1990 On the three-dimensional instability of strained vortices. *Physics of Fluids A: Fluid Dynamics* **2** (1), 76–80.
- WU, C.-C. & ROBERTS, P. H. 2009 On a dynamo driven by topographic precession. *Geophysical and Astrophysical Fluid Dynamics* **103** (6), 467–501.
- WU, C.-C. & ROBERTS, P. H. 2011 High order instabilities of the Poincaré solution for precessionally driven flow. *Geophysical & Astrophysical Fluid Dynamics* **105** (2-3), 287–303.
- WU, C.-C. & ROBERTS, P. H. 2013 On a dynamo driven topographically by longitudinal libration. *Geophysical & Astrophysical Fluid Dynamics* **107** (1-2), 20–44.
- ZAHN, J.-P. 1966 Les marées dans une étoile double serrée. In *Annales d'Astrophysique*, , vol. 29, p. 313.
- ZAHN, J.-P. 1975 The dynamical tide in close binaries. *Astronomy and Astrophysics* **41**, 329–344.
- ZHANG, K., CHAN, K. H. & LIAO, X. 2012 Asymptotic theory of resonant flow in a spheroidal cavity driven by latitudinal libration. *Journal of Fluid Mechanics* **692**, 420–445.